Experimental heat transfer results and flow visualization of vertical upflow boiling in Earth gravity with subcooled inlet conditions – In preparation for experiments onboard the International Space Station

V.S. Devahdhanush[a], Issam Mudawar[a,*], Henry K. Nahra[b], R. Balasubramaniam[b,c], Mohammad M. Hasan[b], Jeffrey R. Mackey[d]

[a] Purdue University Boiling and Two-Phase Flow Laboratory (PU-BTPFL), School of Mechanical Engineering, Purdue University, 585 Purdue Mall, West Lafayette, IN 47907, USA

[b] NASA Glenn Research Center, 21000 Brookpark Road, Cleveland, OH 44135, USA

[c] Case Western Reserve University, 10900 Euclid Ave., Cleveland, OH 44106, USA

[d] HX5, LLC, 3000 Aerospace Parkway, Brook Park, OH 44142, USA

Abstract – Since 2012, researchers at the Purdue University Boiling and Two-Phase Flow Laboratory (PU-BTPFL) and NASA Glenn Research Center have been collaborating on a long-term effort to study flow boiling and condensation in microgravity. The ultimate goal has been to develop the Flow Boiling and Condensation Experiment (FBCE) for the International Space Station (ISS). Based on the findings from prior flow boiling experiments both at different orientations in Earth gravity and onboard parabolic flights simulating short durations of microgravity, a final refined experiment design, construction, and operating procedure have been arrived at for long-duration microgravity flow boiling experiments onboard the ISS. This study investigates flow boiling of n-Perfluorohexane with subcooled inlet in a rectangular channel of dimensions 114.6 mm heated length, 2.5 mm width, and 5 mm height. These pre-launch experiments (Mission Sequence Testing) were conducted in vertical upflow orientation in Earth gravity using the same experimental rig that was launched to the ISS in August 2021. The various operating parameters varied are heating configuration (single- and double-sided), mass velocity (180 – 3200 kg/m^{2}s), inlet subcooling (+0 – 32°C, encompassing both highly subcooled and near-saturated inlet conditions), and inlet pressure (119 – 191 kPa). High-speed video flow visualization images are presented to explain the two-phase interfacial physics within the channel's heated section. Heat transfer results in terms of flow boiling curves, streamwise profiles of wall temperature and heat transfer coefficient, and averaged heat transfer coefficients are analyzed and parametric effects elucidated. Severe temporal thermodynamic equilibrium is observed for near-saturated inlet at very low velocities. Nucleate boiling degradation starts at larger heat fluxes for single-sided heating than double sided at low mass velocities with highly subcooled inlet, and conversely at high mass velocities with near-saturated inlet. Nucleate boiling degradation can be delayed to higher heat fluxes by highly subcooling the inlet and increasing mass velocity. The entire local heat transfer coefficient profiles are degraded at higher heat fluxes for near-saturated inlet, but only the downstream part for highly subcooled inlet. This study also confirmed reliability

of the upcoming ISS experimental data for subcooled inlet conditions and the collected Earth-gravity data will be used for comparison against the ISS data.

Keywords: flow boiling, two-phase heat transfer coefficient, vertical upflow, high-speed photography, subcooled inlet, Earth gravity

* Author to whom correspondence should be addressed; Tel. (765) 494-5705; Fax (765) 494-0539; E-mail: *mudawar@ecn.purdue.edu;* Website: *https://engineering.purdue.edu/BTPFL*

Nomenclature

A	area
A_c	cross-sectional area
Bd	Bond number
Co	confinement number
D_h	hydraulic diameter
G	mass velocity
g	gravitational acceleration
g_e	gravitational acceleration on Earth
μg_e	microgravity
H	height of channel
H_{tc}	conduction length through heating strip
h	enthalpy; heat transfer coefficient
$\overline{h}$	average heat transfer coefficient
h_{fg}	latent heat of vaporization
k	thermal conductivity
L_d	upstream development length
L_e	downstream exit length
L_h	heated length
$\dot{m}$	mass flow rate
N_z	number of streamwise measurement locations
P_h	heated perimeter
p	pressure
q''	heat flux
q''_{CHF}	critical heat flux
q''_{ONB}	heat flux corresponding to ONB
T	temperature
$\overline{T}$	average temperature

ΔT_{sub}	fluid subcooling, $\Delta T_{sub} = T_{sat} - T_f$
t	time
W	width of channel
x_e	thermodynamic equilibrium quality
z	axial coordinate

Greek symbols

ρ	density
σ	surface tension

Subscripts

a	denotes wall 1 or 2 (= 1 or 2)
f	liquid; bulk fluid
g	vapor
h	heated
in	channel heated section inlet
out	channel heated section outlet
s	solid
sat	saturation
sp	single-phase
tc	thermocouple in heated strip
w	wall
wa	wall 1 or 2 (= *w*1 or *w*2)
x=0	corresponding to the location where $x_e = 0$
z	local (along axial direction)

Acronyms

BHM	Bulk Heater Module
CHF	Critical Heat Flux
DC	Direct Current
FBCE	Flow Boiling and Condensation Experiment
FBM	Flow Boiling Module
FDB	Fully Developed Boiling
ISS	International Space Station
MST	Mission Sequence Testing
ONB	Onset of Nucleate Boiling

ONBD Onset of Nucleate Boiling Degradation
PDB Partially Developed Boiling

1. Introduction

1.1 Two-phase Thermal Management of Next Generation Space Vehicles

Many space agencies around the world, especially NASA, are interested in numerous manned and unmanned space missions, which are expected to be for far longer durations and distances, and therefore greatly increase power requirements and weight restrictions. Presently, the thermal management systems used in space vehicles mostly operate on the principles of forced liquid convection. But the design of future space vehicles is accompanied by the need to dissipate larger amounts of heat from smaller device footprints. This points to the need for more advanced cooling solutions.

Two-phase thermal management schemes involving both boiling and condensation have been shown to be advantageous over their single-phase counterparts for various terrestrial applications. Because the two-phase schemes utilize both sensible and latent heat transfer rather than just the former, they are able to yield heat transfer coefficients an order or more in magnitude. By removing large amounts of heat while maintaining the device at a low temperature, boiling schemes could cater to the needs of vehicles used in next generation space missions. Boiling can be implemented in a variety of schemes not limited to capillary [1], falling film [2], pool [3,4], macro-channel flow [5–7], micro-channel flow [6,8–10], jet impingement [11,12], and sprays [13], all of which have been investigated by researchers at the Purdue University Boiling and Two-Phase Flow Laboratory (PU-BTPFL). Each boiling scheme has its own advantages over others but also suffers from limitations. Of all schemes, channel flow boiling is preferred for space applications because of its dependence on flow inertia to remove the vapor produced along the heated wall and simplicity and suitability to cool multiple devices in a fully closed loop while requiring a relatively low pumping power. Aside from the Thermal Control System (TCS) of space vehicles, two-phase flows also have applications in Fission Power Systems (FPS) using the Rankine power cycle [14,15].

1.2 Gravitational Effects on Two-phase Flow and Heat Transfer

With the next-generation space vehicles subject to varying gravity environments, the thermal management system design is more constrained and must be suitable for all gravities. Despite the various aforementioned benefits of two-phase flow heat transfer, the understanding of gravitational effects on both flow patterns and heat transfer is limited.

The considerable influence of gravity on two-phase thermal management schemes has been investigated for many decades. Aside from the comparative experiments at different orientations in Earth gravity [7], researchers have performed microgravity experiments using drop towers [16,17], parabolic flights [17–21], sounding/ballistic rockets [22], and onboard the International Space Station (ISS) [23]. But most microgravity (μg_e) studies [20,21,23–25] have focused on pool boiling. Pool boiling solely depends on buoyancy to remove the vapor produced atop a heated surface. The absence of any forced convection of fluid and thereby a better external mechanism to replenish the heated surface with fresh liquid already results in low critical heat fluxes in Earth gravity. This is further exacerbated in microgravity environments where even buoyancy is negligible, resulting in absence of a means for removing vapor from the surface. A single huge vapor bubble is produced, which covers a significant portion of the surface and results in highly degraded heat transfer performance and low Critical Heat Flux (CHF). Some researchers [26,27] have studied adiabatic gas-liquid two-phase flows in microgravity and realized the vast differences in flow patterns between $1g_e$ and μg_e environments. Of all the classical flow regimes, only bubbly, slug, and annular flows are prominently observed in μg_e.

Very few studies [17–19,28–32] have focused on flow boiling in microgravity. Based on the results of drop tower and parabolic flight experiments, Misawa [17] reported the earlier transition of flow patterns in μg_e than $1g_e$, the diminishing of such effects at high flow qualities, and a lessened bubble-agitation-induced turbulence leading to heat transfer degradation in μg_e. Ohta's [29] μg_e, $1g_e$ (vertical upflow), and $2g_e$ experiments revealed that, at a lower mass velocity of G = 150 kg/m^{2}s, bubbles were larger in μg_e, but at a higher mass velocity of G = 600 kg/m^{2}s, the bubbles detached with roughly the same size in all gravities. This latter similarity was attributed to the higher flow inertia dominating over body force effects by providing enough shear for early detachment of bubbles from the surface. Among their different operating conditions, heat transfer rates were almost unaffected for bubbly flows at all mass velocities, annular flows with moderate inlet qualities and high heat fluxes, and annular flows with high inlet qualities. However, heat transfer degradation was noted in μg_e for annular flows with moderate inlet qualities and low heat fluxes (lower than that required to initiate nucleate boiling) due to the increased thickness of, and reduced turbulence within the annular liquid film. Baltis *et al.*'s [30] parabolic flight experiments showed significantly enhanced heat transfer near the entrance due to larger bubbles in μg_e increasing mixing and turbulence. But higher mass velocities dwarfed body force effects and showed no significant variations in heat transfer. However, most microgravity flow boiling experiments have been of short durations (using drop towers and parabolic flights) and there exists a need to conduct long-duration experiments with a better control of microgravity.

Among the various flow orientations experimented in Earth gravity, *viz*., vertical upflow, vertical downflow, horizontal flow, and other intermediary angles, upflow benefits the most from gravitational effects with the flow being in the same direction as buoyancy. The vapor produced at the heated walls rises upwards and accelerates enhancing flow stability, heat transfer, and CHF [7]. Hence, most Earth-gravity applications are configured to utilize vertical upflow boiling.

As will be detailed in section 1.5, the present study will focus on vertical upflow boiling and serves as a forerunner to the upcoming long-duration microgravity experiments onboard the ISS. In this regard, it is important to note the concurrent efforts to study flow boiling onboard the ISS by another group of researchers through the Japanese Aerospace Exploration Agency (JAXA) [33–35]. Their experiments involve flow boiling of nPFH through a copper heated test tube and a transparent glass heated tube of 4-mm inner diameters. Their research objectives are detailed in [33] and heat loss analysis of ISS data in [34,35].

1.3 Single- and Double-sided Heating of Rectangular Channel

Most flow boiling literary works [36–38] with a focus on gravitational effects were formulated by heating just one wall, *i.e. single-sided heating*. This is to help isolate the effects of different body forces perpendicular and parallel to the heated wall on heat transfer and flow physics. Another reason is to understand the undisturbed evolution of both the bubble boundary layer and the vapor layer. On the other hand, *double-sided heating* (heating of two opposite walls) is more complex because the vapor bubbles produced along both walls interact with each other, changing the flow physics all along the channel. Recent studies [18,19,39] have focused on double-sided heating to understand the interaction effects. For subcooled-inlet flow boiling of FC-72 in microgravity at velocities of 0.1 – 1.9 m/s, Konishi *et al*. [18,19] showed double-sided heating to provide higher CHF values than single-sided for similar inlet conditions. The same conclusion was reached by Kharangate *et al*. [39] for subcooled-inlet horizontal flow boiling of FC-72 in Earth gravity at velocities greater than 1 m/s. Both single- and double-sided heating configurations are considered in this study. Heating more than two of the four walls would compromise the quality of simultaneous flow visualization of the interfacial features while heating by inducing more three-dimensionality, and hence is avoided.

1.4 Subcooled Inlet Conditions

Fluid can be supplied for flow boiling in one of two states: subcooled liquid or saturated liquid-vapor mixture. The flow pattern development and heat transfer physics would be vastly different based on the fluid inlet condition. Note that due to thermodynamic non-equilibrium, especially at conditions very close to liquid saturation ($x_e \rightarrow 0$), the fluid might be subcooled but

still be a two-phase mixture. If the fluid is supplied as a subcooled liquid and the flow channel is long enough, there is possibility for transition from subcooled to saturated flow boiling. However, for a particular heat flux, subcooled boiling is sustained for a longer length upon increasing flow rate, inlet subcooling, and/or diameter [40,41].

The subcooled liquid entering the channel initially undergoes single-phase liquid convection absorbing heat from the walls (*i.e.*, only sensible heat transfer) and increases in temperature. At a certain location corresponding to the Onset of Nucleate Boiling (ONB), the liquid layer close to the wall would have acquired enough superheat for bubble incipience and the first bubbles nucleate. Subcooled boiling commences at the ONB location and extends until the thermodynamic equilibrium quality reaches $x_e = 0$, at which point, the flow regime transitions to saturated boiling. The subcooled boiling region itself can be demarcated into two based on the flow physics: the upstream Partially Developed Boiling (PDB) and the downstream Fully Developed Boiling (FDB) [40,42]. PDB is characterized by the nucleated bubbles still attached to the wall and sliding downstream. The bubbles maintain an almost constant size due to the similar rates of evaporation and condensation, but slight coalescence may be seen. Void fraction increases at a smaller rate due to this appreciable condensation. Liquid convection heat transfer still plays a significant role in PDB, but the flow transitions to FDB at a location where the latent heat transfer overshadows sensible heating. This location corresponds to Net Vapor Generation (NVG) [43] and the first bubbles usually start lifting off the wall. Void fraction increases at a much larger rate due to both weaker condensation effects and activation of more cavities. In the latter part of FDB, especially at high heat fluxes and low pressures, the bubbles may coalesce and form very large irregularly-shaped vapor entities that occupy most of the channel cross-section.

The benefits of flow boiling end at the CHF limit, where the flow transitions to film boiling and the heat transfer coefficient nosedives. This is accompanied by increases in wall temperature to dangerous levels and often leads to device damage and even destruction. For optimum performance and safety, two-phase thermal management systems utilizing boiling must be designed for heat fluxes within the nucleate boiling regime, but safely below CHF.

Overall, subcooled flow boiling offers better heat transfer performance and CHF values than saturated boiling due to (i) the utilization of both sensible and latent heat transfer and (ii) the condensing capability of the subcooled bulk fluid. Only flow boiling with subcooled inlet is considered in this study. Based on the degree of inlet subcooling, for an easier understanding, the experiments have been loosely categorized as *highly subcooled* (roughly $\Delta T_{sub,in} > 10^{\circ}$C) and *near-saturated* (close to saturated liquid state; roughly $0 < \Delta T_{sub,in} \leq 10^{\circ}$C).

1.5 Objectives of Study

The present study is a crucial part of an ongoing long-term collaborative effort between researchers at the Purdue University Boiling and Two-Phase Flow Laboratory (PU-BTPFL) and the NASA Glenn Research Center to study flow boiling and condensation under microgravity conditions. This effort was started in 2012 with an ultimate goal of developing the Flow Boiling and Condensation Experiment (FBCE) for the International Space Station (ISS). Past studies involved flow boiling experiments conducted both in Earth gravity at different flow orientations [39,44–48] and onboard an aircraft performing parabolic maneuvers to simulate short microgravity periods [18,19,49]. The collaborative effort has matured to a point where prior findings have been used to arrive at a final refined experiment design, construction, and operating procedure for long-duration microgravity flow boiling experiments onboard the ISS. FBCE's capabilities, system description, and ISS test matrix are provided in [50].

This study presents results obtained from the final pre-launch experiments (called Mission Sequence Testing, MST) conducted under Earth gravity in vertical upflow orientation using the same experimental rig that was launched to the ISS in August 2021. The present experiments cover a portion of the planned ISS test matrix for subcooled inlet with a focus on the extremes of various operating parameters. High-speed video flow visualization images are presented to explain the two-phase flow physics within the channel for various operating conditions. Heat transfer results in terms of flow boiling curves, streamwise profiles of wall temperature and heat transfer coefficient, and averaged heat transfer coefficients are presented. Parametric effects of heating configuration (single- and double-sided), mass velocity, and inlet subcooling at different inlet pressures are explained. In future studies, the present experimental data will be compared against the upcoming ISS data to clearly show the effects of different gravitational environments on flow boiling heat transfer and fluid physics. For more details on the FBM's CHF results from the MST and corresponding model predictions for subcooled inlet conditions, the reader is referred to [51].

2. Experimental Methods

2.1 Two-Phase Flow Loop

Figure 1 depicts a schematic of the closed two-phase flow loop utilized to condition the working fluid, n-Perfluorohexane (nPFH), to that desired at the inlet of the test module (henceforth called the Flow Boiling Module, FBM). The fluid is positively displaced through the loop using a magnetically-coupled internal gear pump, wherein the fluid is in a subcooled liquid state. For safety purposes, a bypass relief valve is provided across the ends of the pump to let liquid flow back from the high-pressure side (pump outlet) to the low-pressure side (pump inlet) in case the pressure differential exceeds 199.95 kPa (29.00 psid). Another bypass relief valve is provided in parallel to the former and it opens if the pressure differential exceeds 206.84 kPa (30.00 psid). A

Coriolis flow meter downstream of the pump measures the flow rate, which is fed to a flow controller as feedback to adjust the pump head rotation speed to provide the desired set flow rate. After passing through a filter, wherein any possible impurities are removed from the liquid, the subcooled liquid enters the preheater (also called the Bulk Heater Module, BHM), which serves to increase the fluid temperature and produce vapor when necessary. The inlet fluid temperature and quality to the FBM are controlled here based on the amount of heat input from a set of heaters powered by Direct Current (DC) power sources. The preheater is instrumented with thermocouples and Resistance Temperature Detectors (RTDs) that shut the heaters down as a safety measure in case the heating surface exceeds 130°C or the fluid temperature at the heater outlet exceeds 100°C. The subcooled fluid enters the FBM, wherein a finite amount of heat is added to the fluid, based on which, the fluid exits either as a subcooled liquid or a two-phase mixture. This fluid enters a fluid-to-water stainless-steel tube-in-tube heat exchanger (with a spiral-finned inner tube), serving as condenser, wherein it loses heat to the condensing water loop and condenses back to a liquid state and decreases in temperature. The exiting fluid is passed through a static mixer used to continuously mix the liquid without any moving parts; this is done to condense any possible vapor bubbles entrained in subcooled liquid and to ensure thermodynamic uniformity. Consequently, a highly subcooled pure liquid returns to the pump and this helps reduce cavitation and pump head wear down.

Situated immediately downstream of the static mixer is a T-junction where an accumulator is connected to the main flow loop. The accumulator provides a set reference pressure point at the T-junction point of the main loop and helps reduce two-phase flow instabilities in the loop [52,53]. Most of the working fluid resides in the accumulator, on one side of stainless-steel bellows. On the other side of the metallic bellows is air, the pressure and volume of which are controlled by an air pump and a vent valve. A relief valve, set to crack open in case the pressure differential exceeds 137.90 kPa (20.00 psig), is provided next to the vent valve for safety purposes.

The section of the loop between the accumulator T-junction and the pump is split into two parallel paths, with valves routing flow through only one of them. A degassing contactor is provided on one path, while the other is a bypass having no instruments and is used during regular experimentation. The degassing contactor removes all non-condensable gases from the working fluid and helps in the collection of reliable two-phase data. Its main component is a specialized semi-permeable membrane, with fluid flowing on one side and vacuum applied on the other side using a vacuum pump.

The ancillary water loop is equipped with their own flow meters, valves, flow controllers, pressure transducers, and RTDs. Most valves in the flow loop are solenoid actuated to enable remote operation.

2.2 Flow Boiling Module

The primary component of the experimental facility, the Flow Boiling Module (FBM), is made of three transparent Zelux-W polycarbonate plates sandwiched together between two aluminum 7075 support plates. Schematics of the overall construction of the FBM are depicted in Fig. 2(a) and key dimensions given in Table 1. The top and bottom polycarbonate plates are 25.15-mm thick, and the middle plate is 5-mm thick. The 13.72-mm-thick support plates help prevent FBM buckling and fluid leaks by spreading out the bolting stress uniformly across the module. A 5.0-mm deep and 2.5-mm wide rectangular slot is milled into the middle polycarbonate plate to form the flow channel, and a portion of the middle plate is milled further on either side of the channel width to house two oxygen-free copper heating strips (slabs) of dimensions 114.6 mm length, 15.5 mm width, and 1.04 mm thickness. The copper strips are wider than the channel width to effectively embed them within the polycarbonate plates and seal using O-rings. All solid-solid interfaces within the FBM are made leak-proof by using NBR, HNBR, and neoprene O-rings.

The flow channel can be demarcated into three sections: an upstream development length of L_d = 327.7 mm, a middle heated length of L_h = 114.6 mm, and a downstream exit length of L_e = 60.7 mm. The purpose of the development length is to let the flow become hydrodynamically fully developed at the heated length start. The fluid enters and exits the FBM at 90° angles to the flow channel, but the flow streamlines are straightened out and any large eddies broken by affixing a 12.19-mm-thick aluminum 5052 honeycomb insert close to the inlet. For liquid-vapor mixture inlet, the flow straightener reduces swirl effects and improves the vapor distribution throughout the channel cross-section, reducing asymmetricity; the development length further helps the two-phase flow structure be symmetrical and typical of its void fraction.

One side of the heating strips constitutes the heating surfaces and is in contact with the fluid, while on the other side are affixed a set of six thick-film resistive heaters of dimensions 16.4 mm length, 4.5 mm width, and 0.56 mm thickness in series (see Fig. 2(b)). The thickness of copper between the heaters and the fluid heating surface is 0.56 mm. A small separation of 0.9 mm between two successive heaters is provided for thermocouple access to the heating strip; from numerical computations [54], this small spacing has been shown to have virtually no effect on heat flux along the wetted wall due to the very high thermal conductivity of copper. Each heater consists of an aluminum oxide substrate with a 188-Ω resistive layer on its underside stretched between two solder pads. The heaters are soldered to the copper strip to form a solder layer of 96% tin and 4% gold. To ensure uniform heat flux distribution along the copper strip, all heaters are ensured to have very close electrical resistances, are wired in parallel, and powered by DC

power. A maximum power of 175 W per side can be supplied. As detailed in [18,49], this heated wall design allows for fast temperature response and reliable and accurate CHF measurement.

2.3 Instrumentation and Measurement Accuracy

Local pressure measurements are made within the FBM by using five absolute pressure transducers with one each near the inlet and outlet, and three at intermediary locations within the development length as shown in Fig. 1. The fluid temperatures close to the inlet and outlet are measured using type-E thermocouples extending into the flow. As indicated in Fig. 2(c), each heating strip houses two sets of seven type-E thermocouples each to measure the local surface temperatures; the tips of all thermocouples are embedded in shallow holes (resembling hemispherical indentations) made into the strip. One set is used for data collection and software reset of the FBM heater power level in case any temperature exceeds 122°C, usually an aftermath of CHF occurrence. The other set is integral to a hardware safety circuitry and provides feedback to a relay that shuts down the FBM heaters in case the software reset fails and any temperature exceeds 132°C. Local pressures and temperatures are measured and monitored at numerous locations of the flow loop using pressure transducers, and thermocouples and RTDs, respectively.

To conduct both single-sided and double-sided heated wall experiments, power can be supplied to one or both heating strips during testing independent of each other. The electrical power input (as voltages and currents) to each set of FBM heaters and the preheater are measured within the DAQ. Flow rate of the test fluid is measured using a Coriolis flow meter of range 0-60 g/s.

All temporal sensor output signals are collected and measured using a set of two data acquisition systems (2 DAQs; one for thermocouple data and the other for other sensors) at a sampling frequency of 5 Hz during experiments (although all other ‘housekeeping’ data are recorded at a lower rate of 1 Hz). An in-house FBCE flight software is used to monitor and control the DAQs and all other instruments (including solenoid valves). Maximum uncertainties in the measurements of important parameters are given in Table 2.

2.4 Flow Visualization

The intricate interfacial features of two-phase flows are visualized using high-speed photography for all heat flux increments along the boiling curve (both steady-state and CHF). The transparency of the polycarbonate plates allows for excellent visual access to the boiling flow within the FBM’s heated section. All three polycarbonate plates were further vapor polished to minimize vignetting effects produced by the opaque copper heaters and O-rings.

The high-speed camera is directed at one transparent wall with the opposite wall backlit with blue light emitting diodes (LEDs) and a light-shaping diffuser with an intermediate Teflon sheet, which is required due to the extremely short light transmission distance. The camera is equipped with a F#0.95-25 mm lens and captures photographs of resolution 2040×164 pixels at a frame rate of 2000 frames/s and shutter speed of 10 μs. Each pixel on the camera's CMOS (complementary metal-oxide-semiconductor) image sensor is of size 5.5 μm × 5.5 μm and the pixels are arranged with no physical distance between them (*i.e.*, a 100% fill factor). As per spatial resolution tests conducted using the Ronchi ruling (sinusoidal intensity grating), the imaging system was able to achieve a spatial resolution of at least ~90 μm (the system was able to read ~180 μm using the line pair per mm criteria at 50% dynamic range, which is equivalent to ~90 μm spatial resolution per Rayleigh criteria). The heat produced by camera operation is removed from a respective cold plate by the simulated ISS water loop (or by the actual ISS cooling water during the upcoming ISS experiments).

It is noted that all high-speed video images reported in this paper have been uniformly post-processed to make the flow features more distinct.

2.5 Operating Procedure

As already mentioned, the ultimate goal of the present experimental setup is to be installed and tested onboard the ISS and hence, it is to be operated remotely. This means that the entire test matrix must be completed in space without any in-person intervention and both sensor-measured and photography data be transmitted to the personnel on Earth. This study, reporting data from the MST (the final set of experiments in Earth gravity in the vertical upflow orientation), was conducted in the same manner as will be onboard the ISS.

Degassing of the working fluid is performed before the start of testing and on as needed basis. The difference between the measured system pressure at the inlet to the FBM and the saturation pressure gives the partial pressure of any non-condensable gases dissolved in the nPFH. If this partial pressure is greater is 2 kPa, the test fluid is deemed to need degassing and the degassing procedure is invoked. Degassing is needed for both the ground and ISS tests because the experimental system is exposed to air in both environments and there is a possibility of air dissolving in nPFH.

For each boiling curve, the inlet conditions (flow rate, inlet pressure, and inlet subcooling) to the FBM are set and the flow loop allowed to reach them. DC power is supplied to one or both FBM heating strips in small increments starting from zero until CHF is reached. Each heat flux increment is for a fixed time period of 120 s or 180 s, which was deemed sufficient to reach steady state for flow boiling in prior studies [18,49]. Subsequent analysis of collected data revealed that

steady state was indeed reached for all heat flux increments higher than q''_{ONB}. Although CHF is defined as the heat flux increment which causes an unsteady rise in surface temperature, for safety and simplicity, CHF is designated to have occurred at the heat flux increment which causes at least one of the strip thermocouples to exceed 122°C. FBM heater power is brought down to a minimum power level by FBCE software as soon as this limit of 122°C is reached (as measured by the copper-strip data thermocouples). A hardware shutdown of all heaters is invoked at 132°C (as measured by the copper-strip safety-circuitry thermocouples) as a safety precaution to prevent any damage to the FBM (especially thermal deformation or warping of the polycarbonate layers) and to prevent any breakdown of nPFH, which might lead to the formation of the toxic substance perfluoroisobutene (PFiB). All temporal data and high-speed photos are recorded. This procedure is repeated for all predetermined FBM inlet conditions in the test matrix. Note that the actual value of CHF, q''_{CHF}, is the average of the heat flux increment causing the 122°C escalation and the previous heat flux increment that reached steady state.

2.6 Temporal Temperature Records for an Entire Boiling Curve

Temporal variations of fluid inlet, fluid outlet, and heated-strip temperatures are shown in Fig. 3(a) for a representative boiling curve from $q''_w = 0$ to q''_{CHF}. The applied wall heat fluxes correspond to the right axis and the temperatures to the left axis. For the first two heat flux increments, *i.e.*, until about t = 240 s, the strip temperatures keep increasing and never reach steady-state; this transience is greater for the first heat flux increment. Let t_1 denote the latest time instant during the second heat flux increment. During the third heat flux increment, a transient temperature overshoot (also known as *incipient boiling superheat*; this is due to the required superheat for boiling to commence being higher than that to sustain boiling) is observed for both walls; wall 1 shows a slightly bigger overshoot than wall 2. Let t_2 denote the time instant as soon as the overshoot subsides. Fig. 3(b) shows flow visualization images corresponding to both time instants t_1 and t_2, with enlarged half-channel-width photos at three streamwise locations. Clearly, at t_1, heat transfer along the entire channel is solely by single-phase liquid convection, but at t_2, bubbles are seen to nucleate a short distance downstream from the channel entrance. This confirms that the temperature overshoot corresponds to ONB delay. At all heat flux increments higher than the second, nucleate boiling occurs, and all temperatures clearly reach steady state. During the last heat flux increment, at $t \approx 1910$ s, $T_{tc1,6}$ reaches the set maximum operating temperature of 122°C and the heaters are powered down. Note how $T_{tc1,6}$ sharply increases towards the end, clearly indicative of CHF.

Overall, the temporal temperature records corroborate that (i) all heat flux increments with boiling (between ONB and CHF) clearly reach steady state within 120 s and (ii) CHF is indeed reached by the time at least one strip temperature exceeds 122°C.

2.7 Data Processing and Experimental Ranges

Steady state data is extracted from the recorded temporal data by identifying the heat flux increments that reached steady state and averaging the latest 20 s of temporal datapoints of each steady state period. All thermophysical properties of nPFH are obtained from NIST-REFPROP [55]. The fluid enthalpy at FBM inlet (where the fluid is in a subcooled/compressed liquid state) is determined as

$$h_{in} = h\big|_{T_{in}, p_{in}}, \tag{1}$$

where T_{in} and p_{in} are the FBM inlet fluid temperature and pressure, respectively. By performing an energy balance over the FBM, the fluid enthalpy at FBM outlet is calculated as

$$h_{out} = h_{in} + \frac{q''_w P_h L_h}{\dot{m}}, \tag{2}$$

where q''_w is wall heat flux, $\dot{m}$ mass flow rate through the FBM, and P_h heated perimeter determined from channel width, W, as

$$P_h = \begin{cases} W, & \text{single-sided heating} \\ 2W, & \text{double-sided heating} \end{cases}. \tag{3}$$

The FBM was carefully designed to minimize heat loss; except for the fluid heating side, the copper strips are encased on all sides by thick polycarbonate plastic of low thermal conductivity and at the thin heater-and-thermocouple-wire-access slots by stagnant air of low thermal conductivity. An extensive heat loss estimation for a similar test module geometry was performed by Konishi *et al*. [56] in the early stages of FBCE. The older test module differed from the present study's FBM mainly by the older design having only one heating strip to just test single-sided heating, and a comparatively shorter heated length. For both single-phase and two-phase flow situations, heat losses were estimated to be a maximum of 0.2% of electrical power input. This heat loss is well within the maximum uncertainty of heater power measurement (see Table 2) and hence considered negligible. Therefore, all electrical power is considered to heat up the fluid and wall heat flux is calculated by dividing the total electrical power input to the heaters by the fluid heating surface area. Thermodynamic equilibrium qualities at the FBM inlet and outlet are determined from the relation

$$x_e = \frac{h - h_f\big|_p}{h_{fg}\big|_p}, \tag{4}$$

where $h = h_{in}$ or h_{out} is the actual fluid enthalpy at the FBM inlet/outlet, and both h_f, the saturated liquid enthalpy, and h_{fg}, the latent heat of vaporization, are based on the measured inlet/outlet pressure.

The measured heated-strip temperatures, T_{tc}, are translated into the corresponding wall temperatures, T_w, by assuming a uniform heat flux and one-dimensional heat conduction through the copper strip as

$$T_w = T_{tc} - \frac{q''_w H_{tc}}{k_s}, \tag{5}$$

where H_{tc} (= 0.483 mm) is conduction height and k_s pure copper conductivity. T_w is found to be lower than T_{tc} by a maximum of 0.65°C, indicating that the copper conductive resistance between the two points is minuscule. As shown in Fig. 2(c), the local wall temperatures are designated as $T_{wa,z}$, where wa is the heated wall ($w1$ or $w2$) and z the streamwise measurement location (1 upstream through 7 downstream).

The local fluid temperature at these axial locations is determined based on the local state (subcooled or saturated) of the fluid as

$$T_{f,z} = \begin{cases} T_{in} + \left(T_{sat,x=0} - T_{in}\right)\dfrac{z}{L_{h,sp}}, & x_{e,z} < 0 \\ T_{sat,z}, & 0 \le x_{e,z} \le 1 \end{cases}, \tag{6}$$

where heated single-phase length, $L_{h,sp}$, is defined as

$$L_{h,sp} = \frac{GA_c}{q''_w P_h}\left(h_f\big|_{p_{in}} - h_{in}\right), \tag{7}$$

and saturation temperature at the location where $x_e = 0$ is

$$T_{sat,x=0} = T_{sat}\big|_{p_{in}} + \left(T_{sat}\big|_{p_{out}} - T_{sat}\big|_{p_{in}}\right)\frac{L_{h,sp}}{L_h}. \tag{8}$$

Both local saturation temperatures, $T_{sat,z}$, and local thermodynamic equilibrium qualities, $x_{e,z}$, are determined by linear interpolation between values at the inlet and outlet. Local heat transfer coefficient for either wall is defined as

$$h_{a,z} = \frac{q''_{wa}}{T_{wa,z} - T_{f,z}}, \tag{9}$$

and averaged heat transfer coefficient is determined as

$$\overline{h} = \frac{\sum_{N_z} h_{a,z} A_{h,z}}{A_h} = \frac{\sum_{N_z} h_{a,z} L_{h,z}}{L_h}, \tag{10}$$

where $N_z = 7$ is the number of streamwise measurement locations, $A_{h,z}$ and $L_{h,z}$ are, respectively, the heated surface area and length of each unit cell, and A_h and L_h are, respectively, the total heated surface area and total heated length. Averaged wall temperature, $\overline{T_w}$, is also determined in a similar fashion. Ranges of important parameters from the MST experimental database with subcooled inlet are reported in Table 3 for single- and double-sided heating configurations separately. Note that the upcoming ISS experiments would be conducted for roughly the same operating parameter ranges as the MST, but with a much finely-distributed test matrix.

Bond number and confinement number for the FBM's channel, whose hydraulic diameter is $D_h = 3.333$ mm, are respectively calculated as

$$Bd = \frac{\left(\rho_f - \rho_g\right) g D_h^2}{\sigma} \text{ and} \tag{11}$$

$$Co = \frac{1}{D_h}\sqrt{\frac{\sigma}{\left(\rho_f - \rho_g\right) g}} \ . \tag{12}$$

For the present MST experiments, $Bd = 21.49 – 26.19$ and $Co = 0.195 – 0.216$. The very small Co conforms to several different threshold criteria for macro-over-microscale (gravity-over-surface-tension effects dominance) in the literature ($Co < 0.5$ by Kew and Cornwell [57], $Co < 0.79$ by Brauner and Ullmann [58], $Co < 0.57$ by Li and Wang [59], and $Co < 0.3$-0.4 by Ong and Thome [60]; originally proposed values for other dimensionless groups converted to corresponding Co values [60]). This confirms macroscale flow physics within the FBM's channel and less significant surface tension effects.

3. Flow Visualization Results and Discussion

3.1 Flow Visualization for Single-sided Heating

3.1.1 Flow Patterns for Single-sided Heating with Near-saturated Inlet

A schematic representation of single-sided heating configurations is shown in Fig. 4(a). The flow direction is vertically upwards, fully opposing Earth gravity. Heat is added to the fluid from one of the two walls. Figs. 4(b)-(d) portray flow patterns along the boiling curve for near-saturated inlet at mass velocities of $G = 1599.94$ with left wall heated, 1599.94 with right wall heated, and 3199.96 kg/m^{2}s with right wall heated. Included for each operating condition are high-speed video images taken at steady state for heat flux increments from right after ONB until (and including) CHF. The wall heat flux, q''_w, corresponding to each image is mentioned right below it as a percentage of the respective q''_{CHF} for those operating conditions.

In Fig. 4(b), for the heat flux of 10.22% q''_{CHF}, a short upstream single-phase liquid region is observed, after which ONB occurs. This is due to the fluid layers close to the wall needing some heat addition to reach the required superheat for bubble nucleation. Moving downstream, the

bubbles get larger due to the even larger superheat available, activation of more nucleation sites on the wall, and coalescence of neighboring bubbles. The bubbles depart from the wall after reaching a certain size. This typically points to the flow regime becoming fully developed boiling, wherein the net vapor generation is reached, and the effects of single-phase convection diminishes. Since the fluid at inlet is near-saturated, the departed bubbles do not significantly shrink, albeit some condensation does happen at the liquid-vapor interface. Looking at the entire channel length, a bubble boundary layer (the spread of bubbles within the channel) is evolved with a smaller thickness near the entrance and larger thickness (almost the entire channel width) at the exit. As heat flux is increased, the ONB location is seen to move upstream and at 37.54% q''_{CHF}, ONB is right at the inlet and the single-phase liquid length is non-existent. At 25.28% q''_{CHF}, bubble coalescence is much more effective due to the higher heat input from the wall activating more cavities. At 45.28% q''_{CHF}, bubbles coalesce to form larger vapor structures and an almost continuous liquid-vapor interface is observed from about the channel middle. The interface is wavy with crests formed by the vapor and troughs formed by the liquid in contact with the heated surface. These troughs are termed *wetting fronts* and are the primary locations where liquid accesses the wall and boiling continues to occur. As heat flux is increased, the wavy interface formation location moves upstream, all the way to the inlet as seen at 98.55% q''_{CHF}. The vapor crests of these waves also get larger at any axial location as heat flux is increased. The crests even grow large enough to touch the opposite wall as seen near the exit at 53.54% q''_{CHF}. The number of wetting fronts along the wall decrease as q''_w is increased. As shown at 98.55% q''_{CHF}, there is at least one wetting front at about a quarter channel length from the entrance, sustaining boiling. As soon as this vanishes, at 100% q''_{CHF}, CHF is reached, and the wall has no liquid contact. At and after CHF, the heat supplied by the wall is conducted and radiated through the vapor of very low thermal conductivity, and evaporation occurs at the interface; this is representative of *film boiling*. It is noted that, for all heat fluxes, phase change does still occur at the wavy interface and will be either evaporation or condensation depending on local temperatures on either side of the interface.

Fig. 4(c) is for almost the same operating conditions as Fig. 4(b), but with the other wall heated. Note that they both have almost the same q''_{CHF} values. Comparing similar heat flux percentages between these two sub-figures, the flow patterns are almost exactly symmetrical about the channel axial plane. At q''_w = 22.72 – 61.60% q''_{CHF}, although the fluid at inlet is still in a subcooled state with $\Delta T_{sub,in}$ = 3.67°C, there are some small bubbles entering the channel; these are formed within the preheater (BHM) and denote a small thermodynamic non-equilibrium across the channel cross-section. However, as discerned from both these images and the heat transfer results discussed in section 4.1.1, the small non-equilibrium does not significantly affect either

fluid flow or heat transfer. It is noted that, during experimentation, many near-saturated-inlet experiments showed larger non-equilibrium at inlet, and to avoid contaminating the results, the experiments were re-conducted by increasing inlet subcooling by a few degrees Celsius and visually made certain of negligible vapor at channel inlet before collecting data; the only outlier which exhibited severe temporal thermodynamic non-equilibrium at the inlet is discussed in section 3.3.

The mass velocity is doubled to $G = 3199.96$ kg/m^{2}s in Fig. 4(d) and a similar flow pattern progression until CHF is observed, except for the following differences. For a given heat flux percentage, the vapor bubbles are smaller and lesser for higher G; for instance, compare the ~10% q''_{CHF} patterns in Figs. 4(b) and 4(d). The thicknesses of both the bubble boundary layer and wavy interface are also smaller for higher G. For example, compare the ~50% q''_{CHF} patterns in Figs. 4(b) and 4(d), the wavy interface for the smaller G touches the opposite wall, while it does not for the higher. These are all results of the flow inertia being large enough to remove the produced vapor from the channel before large vapor structures can start developing. Even at CHF, the higher G is able to sustain a short single-phase liquid region near the entrance. Note that the flow features for $G = 3199.96$ kg/m^{2}s in Fig. 4(d) are slightly blurred while those for the lower G experiments are crisp; it has been verified from calculations (based on flow velocities, lens magnification, camera pixel element size, and exposure time) that this is not due to *motion blur*, *i.e.*, the camera's shutter speed of 10 μs is sufficient to capture the fast-moving interfacial features corresponding to this highest mass velocity.

3.1.2 Flow Visualization Image Sequences for Single-sided Heating with Near-saturated Inlet

Although the flow patterns at steady-state improve our understanding on how the interfacial features vary for different operating conditions, the steady-state features continuously change with time in a recurring fashion. To better understand this, high-speed video image sequences for near-saturated inlet with single-sided heating are included in Figs. 5(a) and 5(b) for mass velocities of $G = 1599.94$ and 3199.96 kg/m^{2}s, respectively. The images in each sequence are 1.5 ms apart. Two heat fluxes are chosen for all sequential images shown in this study: $q''_w \approx$ 70% and 95% q''_{CHF}; these represent the typical operating heat flux in practical applications and the largest steady-state heat flux just before CHF, respectively. In Fig. 5(a), both at 72.55% and 95.19% q''_{CHF}, the temporal formation and progression of the vapor layer is evident. The vapor layer is formed by the clustering and coalescence of vapor bubbles near the channel entrance. Wetting fronts propagate through the channel gradually shortening downstream as more boiling occurs. The crests of the wavy interface grow both taller and longer due to the accumulation of more vapor. New wettings fronts are formed upstream and the process keeps repeating. In Fig.

5(b), both at 71.44% and 92.47% q''_{CHF}, the same sequential patterns are observed, except that the vapor structures are smaller due to the increased G.

3.2 Flow Visualization for Double-sided Heating

3.2.1 Flow Patterns for Double-sided Heating with Highly Subcooled Inlet

A schematic representation of the double-sided heating configuration is shown in Fig. 6(a). The flow direction is vertically upwards, fully opposing Earth gravity. Heat is added to the fluid from both walls 1 (left) and 2 (right).

Figs. 6(b)-(d) portray flow patterns along the boiling curve until CHF for highly subcooled inlet with double-sided heating at mass velocities of G = 200.01, 1599.94, and 319.98 kg/m^{2}s, respectively. Note that the former two are at lower inlet pressure and the latter one is at higher inlet pressure. For $G \approx 200$ kg/m^{2}s shown in Fig. 6(b), at 16.91% q''_{CHF}, almost no bubbles leave the wall due to the much larger condensing capability of the bulk liquid. This observation even extends to 32.99% q''_{CHF}, where the bubbles are larger than before, but still remain attached to the wall. There are some minute bubbles that have lifted-off the wall, but these are soon engulfed by the highly condensing liquid. As heat flux is increased, massive vapor structures are formed, albeit smaller than in near-saturated fluid. But these structures are more irregularly shaped due to the smaller shear of flow. Continuous wavy interfaces are not formed, but there is a semblance of gear-meshing-type interactions between vapor structures produced at either wall (detailed description in section 3.2.3); for example, see halfway along the channel length at 91.66% q''_{CHF}. Notice at the higher heat fluxes of 90.61 – 100.0% q''_{CHF} how most of the channel downstream is filled with random ripples. Large elongated bubbles at the channel center of roughly the channel diameter, typical of slug flows and annular flows, could have formed at the channel center, and the ensuing interfacial turbulence caused by the large velocity difference between the fast-moving central core and slow moving annular liquid film could be the cause of the photographed ripples. Notice at 100% q''_{CHF}, the presence of a darker strip halfway within the downstream lighter ripply region; this is most probably indicative of a liquid slug between two large vapor bubbles or a *high-density liquid front* in Density Wave Oscillations (DWOs). The CHF mechanism here is totally different and not due to the extinguishing of wetting fronts.

The higher mass velocity ($G \approx 1600$ kg/m^{2}s) case shown in Fig. 6(c) exhibits remarkably different flow patterns than any of the operating conditions discussed in this study. Heat fluxes until 55.69% q''_{CHF} show minuscule bubbles near the walls, with the number of these bubbles higher at higher heat fluxes. After lifting off the walls, these bubbles disappear almost instantly for heat fluxes up until 27.94% q''_{CHF}. These are all due to the far greater condensing capability and sensible heat transfer, the latter being extremely dependent on flow rate. Bubbles start getting

larger from heat fluxes of 67.99% q''_{CHF}, but again the lifted-off bubbles are minuscule due to extreme condensation. At 80.09% q''_{CHF}, large vapor structures are formed near the channel exit. At higher heat fluxes up until and including CHF, long continuous vapor layers form on both walls with wetting fronts as discussed for the near-saturated cases. But the differences here are the almost unapparent gear-meshing behavior of the two interfaces, the very large wavelengths of the interfaces, and a continuous liquid stream from the inlet to exit even at CHF. This is again attributed to large flow inertia and condensation at the liquid-vapor interface.

The higher-inlet-pressure higher-mass-velocity flow patterns shown in Fig. 6(d) are similar to the flow patterns shown in Fig. 6(b). Note the fuzziness in the high-speed video images very close to the two heated walls; this is due to vignetting effects. Some aspects contributing to overall vignetting are (i) the opaque copper heater strip sandwiching the flow channel and (ii) the black O-rings between each polycarbonate boundary. Vignetting is more pronounced near the right wall due to the high-speed camera's image readout not physically being at the exact center of the channel although the images are centered.

3.2.2 Flow Visualization Image Sequences for Double-sided Heating with Highly Subcooled Inlet

High-speed video image sequences for double-sided heating with highly subcooled inlet are included in Figs. 7(a) and 7(b) for mass velocities of G = 200.01 and 1599.94 kg/m^{2}s, respectively. The images in each sequence are 5.0 ms apart. In Fig. 7(a), at 69.74% q''_{CHF}, as time advances, the vapor bubbles move downstream gradually increasing in size due to more boiling and coalescence. But at 94.78% q''_{CHF}, the size increase is faster due to the increased heat flux and more phase change. Notice the middle of the channel, a huge bubble is formed at about the middle time instance, and this bubble increases in size in both directions as time advances. This is due to low liquid inertia. The darker region downstream of this bubble is similar to a liquid slug in typical slug/churn flow regime; the presence of entrapped irregular vapor entities here indicates a more churn-like flow. Downstream of this slug, near the channel exit, is another huge vapor bubble at the channel center.

In Fig. 7(b), at 67.99% q''_{CHF}, due to the higher mass velocity of $G \approx 1600$ kg/m^{2}s, only discrete bubbles are seen throughout the channel, but they grow in size as time advances. But before they can coalesce to form large vapor structures, they are pushed out of the channel. On the other hand, 91.47% q''_{CHF} shows an interesting recurring pattern. At the first time instance shown, a long continuous interface that insulates nearly three-fourths of the heated wall downstream is seen. As time advances, this long vapor layer is gradually pushed out and smaller bubbles nucleate. The bubbles gradually grow in size all along the channel and the liquid between

the vapor structures decrease in size due to more boiling. At one point, a roughly continuous wavy interface is formed, whose thickness decreases and wavelength increases due to the fast-moving highly-condensing liquid at the channel center. And the events repeat.

3.2.3 Flow Patterns for Double-sided Heating with Near-saturated Inlet

Figs. 8(a)-(c) portray flow patterns along the boiling curve for near-saturated inlet with double-side heating at mass velocities of G = 199.98, 1599.94, and 3199.97 kg/m^{2}s, respectively. Included for each operating condition are high-speed video images taken at steady state for heat flux increments from right after ONB until (and including) CHF.

In Fig. 8(b), at the lowest heat flux of 14.17% q''_{CHF}, bubbles nucleate from both walls; but the overall pattern is similar to the single-sided heating pattern shown in Fig. 4(b) for the similar operating conditions. It may seem that the left wall is producing more vapor than right, but this is due to slight differences in heat fluxes between the two walls. Downstream of the channel, the bubble boundary layers from both walls merge with one another. This interaction becomes stronger at higher heat fluxes, wherein the wavy interfaces start interacting with one another. Notice at 36.41% q''_{CHF}, near the channel exit, the liquid at the channel center has to take a serpentine path confined between the wavy interfaces of both walls. Also notice that both wavy interfaces mate with each other similar to the meshing of gear teeth. The location of onset of this wave interaction moves upstream as heat flux is increased. At 52.22% q''_{CHF}, the two interfaces almost fully merge near the channel exit. The location of merging also moves upstream as heat flux is increased; notice at 99.33% q''_{CHF} how the merging is complete at around the middle of the channel. It is noted that since the true flow features have an element of three-dimensional chaos, a characteristic of the churn flow regime, the two-dimensional high-speed video images might not be able to confirm features such as *complete merging* and so on. For example, even after merging seems to be complete in these images, a dark wave runs along the channel till the exit; this indicates that liquid still flows along the dark wave, possibly at a depth of $H/2$ (half the channel height) beneath the imaging wall.

The highest mass velocity ($G \approx$ 3200 kg/m^{2}s) case shown in Fig. 8(c) varies from the moderate mass velocity ($G \approx$ 1600 kg/m^{2}s) case in Fig. 8(b) in the same manner the single-sided cases vary between Figs. 4(b) and 4(d) for the same operating conditions. The higher flow inertia makes both the bubble boundary layer and the vapor layer thinner.

The lowest mass velocity ($G \approx$ 200 kg/m^{2}s) case portrayed in Fig. 8(a) shows significantly different behavior compared to $G \approx$ 1600 and 3200 kg/m^{2}s. It is emphasized that this experimental case exhibited temporally anomalous flow, which will be discussed in detail in section 3.3, and images representative of the flow at each heat flux increment are shown here. Due to the increased

residence time of the fluid at lower flow rates and the negligible condensing capability of near-saturated fluid, the bubbles are much larger; compare the ~14% q''_{CHF} patterns in Figs. 8(a), 8(b), and 6(b). Almost all bubbles are irregularly shaped. Even at a small heat flux of 22.75% q''_{CHF}, bubbles occupy the entire channel a short distance from the entrance. Large vapor structures, filling almost the entire channel width, are observed. Unlike the higher mass velocities, a continuous long vapor layer never forms along the walls. There are indications of a subtle short vapor layer forming near the entrance for heat fluxes 66.79 – 100.0% q''_{CHF}. However, they completely merge after a very short distance. Notice at the heat fluxes of 77.01 – 100.0% q''_{CHF} how most of the channel downstream is filled with random ripples; as already described for Fig. 6(b), the downstream churn-flow-like flow regime's three dimensionality deters us from further interpretations of flow physics.

3.2.4 Flow Visualization Image Sequences for Double-sided Heating with Near-saturated Inlet

High-speed video image sequences for double-sided heating with near-saturated inlet are included in Figs. 9(a) and 9(b) for mass velocities of G = 1599.94 and 3199.97 kg/m^{2}s, respectively. The images in each sequence are 1.5 ms apart. The temporal evolution of gear-teeth meshing pattern of wavy interface is clearly seen in these images. The vapor layers on both walls compete with each other trying to occupy the entirety of channel. The peak of one layer dominates, grows outward and compresses the other layer. Immediately, the other layer pushes back with its own wave peak which grows and dominates the other. This process repeats. The two interfaces are separated from each other by the central liquid layer. Note that, particularly downstream and at high flow velocities, small bubbles may be seen entrapped within the liquid layer; these bubbles are the result of the liquid shear acting on the vapor layer both shattering the peaks and helping eject nucleated bubbles from the wall within the troughs. The thickness of the liquid layer decreases downstream and culminates in complete merging of the two vapor layers and a churn-flow-like chaotic downstream region occupied by mostly vapor with traces of liquid.

3.3 Image Sequences Portraying Temporally Anomalous Flow for Certain Operating Conditions

Although almost all operating conditions in this study behaved as expected, certain specific operating conditions (near-saturated inlet at low flow rates with either single- or double-sided heating) exhibited severe temporally anomalous flow. Flow visualization image sequences for near-saturated inlet with double-sided heating at a low mass velocity of G = 199.98 kg/m^{2}s are portrayed in Fig. 10. To understand a full cycle of recurring flow behavior, the time interval between images in each presented sequence is much longer at 25 ms.

At the much lower heat flux of q''_w = 12.25% q''_{CHF}, the first image indicates an almost normal flow pattern with bubbly flow all along the channel with coalescence resulting in larger bubbles downstream; this is true with the exception of the elongated bullet-shaped bubble, having a diameter slightly smaller than that of the channel cross-section and typical of those observed in the slug flow regime, entering the channel. As time advances, this bubble moves downstream along with the general flow, engulfing all the smaller bubbles that nucleate at the walls, the annular liquid film surrounding it evaporating, and growing in length gradually. Soon after, more elongated bubbles enter the channel indicating the slug flow regime. The liquid slugs have smaller bubbles resulting from both the tail of the larger bubbles breaking away and nucleation occurring at the walls. However, these bubbles are much smaller than those observed in the first image. The length of the elongated bubbles entering the channel does not seem to follow any fixed pattern as the length increases for the first three bubbles, but they are followed by two very short bubbles (resembling caps) and lastly by a very long bubble filling the entire channel length. This last flow pattern is indicative of the annular flow regime. The thin annular liquid film surrounding both the slug-flow-regime's elongated bubbles and the annular-flow-regime's vapor core evaporates and reduces in thickness, typically resulting in high heat transfer. Soon after, as seen in the fifth image from the right, liquid comes gushing in, resulting in boiling and the entire cycle repeats. This recurring introduction of liquid prevents dryout of the annular liquid film. The alternating events characterized by nucleate boiling, convective boiling, and thin-film evaporation results in very high average heat transfer coefficients than those typically expected for these operating conditions (from predominantly nucleate boiling), as will be evident in section 4.4.

A similar cycle of events is observed at the higher heat flux of 96.28% q''_{CHF}, with the following differences. Since the exit quality for this case is already high at $x_{e,out}$ = 0.415, all the incoming vapor merges with the large quantity of vapor already present within the channel and results in fully annular flow, and not result in elongated bubbles. Notice the three periods of fully annular flow in the sequences: the first for ~2 images, the second for ~2 images, and the third ~4 images; this is a direct manifestation of the amount of vapor entering the channel, which is smaller for the first two and larger for the last one. However, heat transfer is not significantly augmented at higher heat fluxes since convective boiling already plays the dominant role here.

The authors believe the reasons for this temporally anomalous flow behavior are the alternating introduction of vapor and liquid from the preheater resulting in severe temporal thermodynamic non-equilibrium (even though the temporal average at steady-state indicates an inlet subcooling of $\Delta T_{sub,in}$ = 2.60°C) and possible Density Wave Oscillations (DWO), a type of two-phase instability. Although this temporal behavior is evident from the high-speed videos recorded at 2000 fps, further analysis is out of the scope of the present study. For further details

on DWO, the reader is directed to the studies by O'Neill *et al*. [61,62], who explicitly addressed DWO for this flow geometry by collecting pressure signals at a much higher sampling rate of 200 Hz compared to the 5 Hz in this study. It is to be seen whether microgravity also results in such severe temporal flow anomalies for these operating conditions.

4. Heat Transfer Results and Discussion

Heat transfer results in terms of flow boiling curves, wall temperatures, and heat transfer coefficients are presented in this section and discussed.

4.1 Flow Boiling Curves

Boiling curves are an excellent way to show the heat transfer performance of a two-phase thermal management system. All boiling curves included in this study are plotted as wall heat flux against average wall superheat, which is defined as the average wall temperature, $\overline{T}_w$, minus the inlet fluid saturation temperature, $T_{sat,in}$. As already discussed, the focus of this study is the two-phase heat transfer region, the lower limit of which is the ONB and the upper limit the CHF. Although these curves start after ONB is observed at any location of the channel, all boiling curves in this study do show an increase in slope at a low heat flux. This corresponds to the point where latent heat transfer starts to dominate over sensible heat transfer; and not where ONB occurs; this is due to these being averaged boiling curves for the entire heated wall and not a single location on the wall. For example, consider a flow situation in which the single-phase liquid convection regime occupies most of the channel and ONB observed at a downstream location with partially developed subcooled boiling (PDB) downstream of ONB; this flow situation would result in an overall sensible heat transfer dominance although boiling does occur for a portion of the channel.

4.1.1 Single-sided versus Double-sided Heating

Boiling curves illustrating the effects of heating configuration are shown in Figs. 11(a) and 11(b) for two combinations of mass velocity and inlet subcooling: highly subcooled at low *G* and near-saturated at high *G*, respectively. Shown in each plot are separate boiling curves for each heated wall for the same set of operating conditions. The double-sided heating configuration has two curves while the single-sided one.

Note that two single-sided configurations are shown in each plot; these experiments were conducted by heating either wall 1 (left) or 2 (right) and analyzing data corresponding to the respective heated wall. Both Figs. 11(a) and 11(b) show boiling curves for both single-sided configurations almost lie on top of each other with the same q''_{CHF}. This is suggestive of flow being almost perfectly symmetrical about the channel central plane and there being no bias

between the two heated walls, as it should be for vertical upflow. There is a slight difference in q''_{CHF} in Fig. 11(b), but since the last steady-state point of both curves are almost of the same heat flux, this can be attributed to a small CHF isolation error for the wall 2 heated case. All other single-sided experiments in this study were conducted by heating wall 2 only.

Again, both the boiling curves for double-sided heating fall onto one another, further confirming heat transfer symmetry. The nucleate boiling portion of both single- and double-sided curves overlap, but after the Onset of Nucleate Boiling Degradation (ONBD), the curves diverge. ONBD is defined as the heat flux after which the slope of the boiling curve changes after the almost linear trend exhibited by nucleate boiling (note that some studies have termed ONBD as *dryout incipience*) [12,63]. Increasing the heat flux after ONBD results in much larger wall temperature increases due to intermittent wall dryout and heat transfer coefficient degradation. Fig. 11(a) and 11(b) show different contradictory behavior as to which heating configuration sustains nucleate boiling for a larger heat flux. The highly subcooled low mass velocity case has the single-sided heating sustain heat transfer performance for a higher heat flux than double-sided; single-sided also yields a higher q''_{CHF} than double-sided. This can be explained by the higher residence time of the fluid within the heated section at low flow rates. Note that for the same heat flux, double-sided heating dumps twice the amount of heat to the fluid than single-sided owing to its double heating surface area. This means that the double-sided is adding more heat to the fluid leading to more evaporation and a higher void fraction at any channel axial location. This larger void for double-sided coupled with the much lower inlet G leads to the earlier flow regime transition to slug flow, wherein the CHF mechanism is different as observed in Fig. 6(b) and described in section 3.2.1.

On the other hand, the near-saturated high mass velocity cases in Fig. 11(b) have a slightly better heat transfer performance and higher q''_{CHF} for double-sided heating than single-sided. The produced vapor remains within the channel until they are pushed out due to the near-saturated fluid offering negligible condensation. Owing to the much higher fluid velocity, wavy interfaces with wetting fronts are formed as observed in Fig. 8(b). The larger void from double-sided heating accelerates the flow, while still maintaining wavy interfaces with wetting fronts and this prolongs nucleate boiling and enhances q''_{CHF}. A similar effect was observed by Konishi *et al*. [18] for near-saturated-inlet flow boiling in microgravity.

4.1.2 Mass Velocity Effects

Boiling curves illustrating the effects of mass velocity are shown in Figs. 12(a) and 12(b), for highly subcooled inlet with single-sided heating and near-saturated inlet with double-sided heating, respectively. In Fig. 12(a), for all mass velocities except $G \approx 2400$ kg/m^{2}s, the lower

portions of the boiling curves overlap due to the independence of latent heat transfer on fluid flow rate. Higher G is able to sustain nucleate boiling for larger heat fluxes, delaying ONBD. This is due to the higher fluid inertia removing produced vapor along the heated wall and replenishing it with fresh liquid for more nucleate boiling. The same reasoning is behind the higher q''_{CHF} at higher G. Note that for the highest G of 2399.99 kg/m^{2}s, CHF was not attained even with maximum heat output from the FBM heaters.

Fig. 12(b) shows similar trends for the near-saturated inlet cases with double-sided heating. For all mass velocities, the lower portions of the curves overlap. It is apparent that q''_{CHF} does not increase linearly with G. For example, increasing G from 480.02 to 2400.00 kg/m^{2}s, a 400% increase, enhances q''_{CHF} from 26.10 to 41.58 W/cm^2, a 59.31% increase. This means that in an actual application, the higher pumping power necessary for higher G should be weighed against the ameliorated q''_{CHF} it yields.

The key takeaway is increasing G raises the upper limit of cooling, the CHF, but it does not have any effect on the wall temperature for steady-state nucleate boiling.

4.1.3 Subcooled Inlet Conditions: Inlet Subcooling Effects

The effects of inlet subcooling on the boiling curves are shown in Figs. 13(a) and 13(b), for single- and double-sided heating, respectively. Shown in each plot are subcooling effects at the experimented mass velocity extremes of $G \approx 200$ and 3200 kg/m^{2}s. Fig. 13(a) shows the enhanced heat transfer performance offered by highly subcooled fluid over near-saturated inlet (low subcooling) for both mass velocities. For a given wall superheat, higher subcooling is able to dissipate higher heat fluxes owing to better condensation and larger sensible heat transfer. Fig. 13(b) shows similar trends for double-sided heating, with an even closer clustering of curves in the nucleate boiling region.

Both the highest heat transfer performance and the highest q''_{CHF} are obtained with highly subcooled liquid delivered at large mass velocity.

4.2 Local Wall Temperature

Streamwise local wall temperature ($T_{w,z}$) profiles are included in Fig. 14 for different heat fluxes with both single- and double-sided heating configurations at a variety of operating conditions. The plots on the left correspond to single-sided heating and those on the right double-sided for similar operating conditions. Four different sets of operating conditions are examined; respectively from the top to bottom are plots for low-mass-velocity highly-subcooled fluid at low inlet pressure, low-mass-velocity near-saturated fluid at low inlet pressure, high-mass-velocity near-saturated fluid at low inlet pressure, and high-mass-velocity near-saturated fluid at high inlet

pressure. Within each plot are included $T_{w,z}$ profiles for heat fluxes ranging between ONB and CHF as percentages of q''_{CHF}.

At each streamwise location, the wall temperature monotonically increases with increasing heat flux. The low heat flux profiles are rather flat indicating uniform wall temperature. But as heat flux increases, the profiles take a concave-downward shape with the concavity increasing with increasing heat flux. This indicates the maximum T_w to be at a location ranging from the middle to just before the downstream end of the heated wall (to be precise, measurement locations 4 to 6 in Fig. 2). T_w is lowest near the inlet due to the inlet fluid temperature being subcooled and the lowest along the channel. T_w increases thereafter due to the fluid gradually gaining heat from the wall as it moves downstream, the development of thermal boundary layer, and the development of vapor layer. The flow being vertically upwards, the produced vapor accelerates due to both buoyancy and specific volume increase. This results in the overall increased flow velocity downstream which enhances convective heat transfer, turbulence, fluid mixing, and removal of produced vapor from the channel. These effects due to flow acceleration effectively dominate over the effects of fluid heat gain and vapor layer development, and lead to a decrease in T_w. Another possible reason for lower T_w at both ends of the heated section is the extended heat transfer area covered by the end resistors, resulting in a slightly lower heat flux at both ends compared to the majorly uniform heat flux for the length of the heated section. This further indicates that CHF occurs in this region of maximum T_w, which has been confirmed in previous studies [18,19]. The location of maxima of $T_{w,z}$ profiles seems to be sharp (*i.e.*, well defined at a particular location) and downstream (measurement location 6) for highly subcooled inlet (row 1) and is rather flat and spread over the middle-to-downstream (measurement locations 4 to 6) for near-saturated inlet (rows 2-4). This is directly attributed to the degree of fluid subcooling, which when high, has greater condensing capability and hence can absorb most of the produced vapor and defer flow acceleration effects to the downstream, where the fluid has absorbed enough heat for it to lose most of its condensing capability.

Comparing the single-sided (left) and double-sided (right) plots in each row, the profile trends are almost the same. The slight deviations are due to (i) double the wall surface area and double the amount of heat addition to fluid for a heat flux, (ii) more vapor production leading to larger acceleration effects, especially downstream, and (iii) the interaction between vapor layers formed at both walls leading to increased fluid mixing and turbulence. Comparing the two heated walls in double-sided heating, most profiles overlap onto each other. Sometimes, one wall's temperature is slightly higher than the other due to minor differences in the heater resistivity and slightly preferential vapor production. Notice for the high-mass-velocity cases (rows 3,4 on right), at heat fluxes especially greater than ~65% q''_{CHF}, the upstream T_w (particularly for measurement

locations 1 and 2) is significantly different for the two walls, *i.e.*, $T_{w1} > T_{w2}$. As verified from the corresponding heat flux images in Fig. 8(c), this could be due to the comparatively thicker and more continuous vapor layer on wall 1 (left) than wall 2. This results in the inability of the liquid to access and effectively cool wall 1 and more axial heat conduction from the downstream. But nucleate boiling still occurs on wall 2 and the wetting fronts in the vapor layer are slightly more, resulting in more cooling and lower T_w upstream.

4.3 Local Heat Transfer Coefficient

4.3.1 Streamwise Local Heat Transfer Coefficient Profiles

Streamwise local heat transfer coefficient (h_z) profiles are included in Fig. 15 for different heat fluxes with both single- and double-sided heating configurations at a variety of operating conditions. The layout of the overall figure and operating conditions and heating configurations of each plot are the same as Fig. 14. Overall, the single- and double-sided heating configurations yield similar h_z profiles except for minor differences for the same reasons described in section 4.2.

For highly subcooled inlet (row 1), h remains almost constant along the flow direction at lower heat fluxes. And h monotonically increases as heat flux increases at the first two upstream locations. These are due to the highly subcooling of the fluid quickly condensing all produced vapor, resulting in a very similar bubble layer all along the channel; see the corresponding flow patterns in Fig. 6(b). At moderate heat fluxes, as latent heat transfer starts dominating and flow accelerates, h monotonically increases along the channel. But this monotonicity ceases at some axial location for higher heat fluxes due to the massive coalescence of produced vapor, formation of large vapor structures, and decrease in liquid available for boiling; this axial location moves upstream for higher heat fluxes. Notice how flow acceleration effects still try to enhance heat transfer downstream even for the highest heat flux.

For near-saturated inlet (rows 2-4), each h_z profile overall follows the same trend: a decrease near the channel entrance, constant in the middle, and an increase near the exit. The decrease is due to the development of both the thermal boundary layer and bubble boundary layer. The increase downstream is due to the flow acceleration effects already described. Only at the lower heat fluxes, the entire h_z profile monotonically increases with increasing heat flux. The higher heat fluxes show a different behavior. At moderate-to-high heat fluxes, the h_z profiles are degraded in the same manner as for highly subcooled inlet, *i.e.*, degradation starts at some location along the channel. But, at the highest heat fluxes, especially close to CHF, the entire h_z profiles are degraded; notice how the 94.53% q''_{CHF} profile (left row 2) is the lowest among all. The higher G cases (rows 3,4) do not show this degree of h degradation due to the fluid's lower channel residence time and higher effectiveness in vapor layer removal and liquid replenishment.

4.3.2 Local Heat Transfer Coefficient Variations with Local Thermodynamic Equilibrium Quality

Variations of local heat transfer coefficient (h_z) with local thermodynamic equilibrium quality (x_e) are shown in Fig. 16 for different heat fluxes with both single- and double-sided heating configurations at a variety of operating conditions. The layout of the overall figure along with the operating conditions and heating configurations of each plot are consistent with Figs. 14 and 15. Note that the horizontal axes are not identical for all plots, but are dependent on both $x_{e,in}$ and heating configuration. It is emphasized that x_e is not equal to vapor quality due to the high inlet subcoolings and high mass velocities tested in this study. Except for very few cases such as near-saturated inlet with low mass velocities, the curves almost entirely span negative x_e values, meaning that thermodynamic non-equilibrium plays a vital role in determining the heat transfer mechanism and associated h_z. This means that two curves might have different vapor qualities, flow regimes, and heat transfer mechanisms for the same x_e.

For highly subcooled inlet (row 1), both single- and double-sided heating yield curves that are flat at lower x_e due to the dominance of nucleate boiling heat transfer, which also causes h_z to monotonically increase with heat flux. Beyond a certain x_e, h_z increases with increasing x_e due to the increased contribution of convective boiling (*i.e.*, film evaporation), which also reduces the dependence of h_z on heat flux. At very high heat fluxes, the curves are seen to slightly decrease and become flat at high qualities due to the possible formation of intermittent dryout patches within the channel, which negatively affects h_z. For near-saturated inlet (rows 2-4), h_z is high at qualities very close to the inlet quality due to the entrance effects already discussed. One other possible reason for high h_z near the inlet and outlet is the extended heating surface area covered by the end resistors as already discussed in section 4.2. The other trends follow prior discussions. For near-saturated inlet at high mass velocities (rows 3 and 4), the practical decrease in inlet quality with increasing heat flux coupled with the very small increase in x_e from the inlet to the outlet makes it difficult to discern any trends with respect to heat flux.

For all operating conditions, heating configuration negligibly affects the trends of the curves, but the curves span a larger x_e range for double-sided heating due to heat addition from both walls.

4.4 Average Heat Transfer Coefficient

Average heat transfer coefficient ($\bar{h}$) variations with wall heat flux are shown in Fig. 17 for both single- and double-sided heating at four different inlet conditions (two inlet subcoolings × two inlet pressures). The top two rows correspond to low inlet pressure and the bottom two rows

to high inlet pressure. Among these, the top plots (rows 1,3) correspond to highly subcooled inlet and the bottom plots (rows 2,4) correspond to near-saturated inlet. Included in each plot are curves for different mass velocities.

For all operating conditions, the curves show a common behavior: an almost linear increase in $\bar{h}$ at low heat fluxes, a peak, and a decrease at heat fluxes close to CHF. The initial increase is due to the increased contribution of latent heat transfer due to boiling in addition to the almost-constant sensible heat transfer. Notice how this increasing region is larger and more linear for highly subcooled inlet than near-saturated; this is due to the produced bubbles quickly collapsing within the bulk fluid as already described. The peak $\bar{h}$ value does not follow any fixed trend with respect to *G*; see how the extreme *G* of 200 and 3200 kg/m^{2}s roughly yield the highest peak $\bar{h}$ for highly subcooled inlet and a moderate *G* of 1600 yields the highest peak $\bar{h}$ for near-saturated inlet. But, at higher *G*, the location of the peak $\bar{h}$ is observed at higher heat fluxes. It is clear the near-saturated inlet cases yield higher peak $\bar{h}$ than the highly subcooled cases due to the nucleate boiling from the lower heat fluxes keeping the wall temperature closer to the fluid's. On the other hand, the highly subcooled cases required the wall to be a certain temperature higher than the fluid saturation temperature for boiling to occur while the bulk fluid temperature is really low; this large difference between T_w and T_f leads to lower $\bar{h}$. Nonetheless, the highly subcooled cases do have the capability of dissipating more heat as deduced from the q''_{CHF} values. Finally, the $\bar{h}$ decrease at higher heat fluxes indicates heat transfer degradation for reasons discussed in section 4.3; closer to CHF, h_z degradation is severe throughout the entire channel leading to a minimum $\bar{h}$.

Notice the odd trend for the lowest *G* of 200 kg/m^{2}s with near-saturated inlet (row 2); both single- and double-sided configurations show local $\bar{h}$ maxima for the lowest heat flux and $\bar{h}$ decreases to minima before increasing as seen for the other curves. As already mentioned in section 3.3, these experiments exhibited severe temporal thermodynamic non-equilibrium and two-phase instabilities. The recurring introduction of intermittent large bullet-shaped elongated vapor bubbles (typical of both slug and annular flows, occupying almost the entire channel cross-section) and their slow passage through the channel causes enhanced heat transfer due to the wall heat flux causing evaporation of the thin liquid layer surrounding the vapor and convective boiling in addition to new bubble incipience. This could lead to a much higher $\bar{h}$ for very low heat fluxes for this set of operating conditions. But as heat flux is increased, where convective boiling is already dominant, these effects diminish and the usual flow physics dictate heat transfer rates as deduced from the $\bar{h}$ curves following the same trends as all other operating conditions.

Overall, both single- and double-sided heating (as well as the two walls for double-sided) configurations show similar trends with minor differences that can be explained by the reasons

discussed in section 4.2. Although the two inlet pressures do not allow for direct comparison due to the experimented mass velocities being different, the overall trends remain the same for both.

5. Conclusions

This study explored subcooled-inlet flow boiling of nPFH based on results obtained from the final pre-launch Earth-gravity Mission Sequence Tests (MSTs) of NASA's Flow Boiling and Condensation Experiment (FBCE) that was launched to the International Space Station (ISS) in August 2021. The experiments were conducted using the Flow Boiling Module (FBM) in vertical upflow orientation with both single-sided and double-sided heating and covered a portion of the planned ISS test matrix for subcooled inlet with a focus on the extremes of various operating parameters. High-speed video flow visualization images were presented to explain the interfacial features within the channel. Parametric effects of mass velocity, inlet subcooling, and heating configuration (single- and double-sided) at different inlet pressures on both flow visualization and heat transfer results were explained.

Key observations from the present experiments have been summarized in Table 4. Differences in various aspects of this study (*viz*., evolution of bubble boundary layer and vapor layer, local wall temperature, local heat transfer coefficient, average heat transfer coefficient, and ONBD and CHF) have been noted for different heating configurations, degrees of inlet subcooling, and mass velocities. Operating conditions with near-saturated inlet at very low velocities exhibited severe temporal thermodynamic non-equilibrium. Overall, MST of the FBCE's FBM was successful for subcooled inlet conditions. The ISS-intended experimental facility worked as expected and further analysis of all sensor-measured and flow visualization data confirmed reliability of the upcoming ISS data.

Declaration of Competing Interest – None. The authors declare that they have no known competing financial interests or personal relationships that could have appeared to influence the work reported in this paper.

Acknowledgement – The authors are appreciative of the support of the National Aeronautics and Space Administration (NASA) under grant no. NNX17AK98G. The authors are also thankful to the FBCE personnel at NASA Glenn Research Center, Cleveland, Ohio, especially Nancy Hall (FBCE Project Manager), Rochelle May and Phillip Gonia (Software Engineering), Mark Sorrells (Assembly, Integration and Test Lead), Jesse DeFiebre (Fluids Lead), Monica Guzik (FBCE Chief Engineer), and ZIN FCF Mission Operations Team, for their dedicated technical assistance and successful completion of the MST. This work was also partly supported by Purdue University's Bilsland Dissertation Fellowship.

References

[1] T.J. LaClair, I. Mudawar, Thermal transients in a capillary evaporator prior to the initiation of boiling, Int. J. Heat Mass Transfer 43 (21) (2000) 3937–3952, doi: 10.1016/S0017-9310(00)00042-9.

[2] I. Mudawar, R.A. Houpt, Mass and momentum transport in smooth falling liquid films laminarized at relatively high Reynolds numbers, Int. J. Heat Mass Transfer 36 (14) (1993) 3437–3448, doi: 10.1016/0017-9310(93)90162-Y.

[3] I. Mudawar, T.M. Anderson, Parametric investigation into the effects of pressure, subcooling, surface augmentation and choice of coolant on pool boiling in the design of cooling systems for high-power-density electronic chips, J. Electron. Packag. 112 (4) (1990) 375–382, doi: 10.1115/1.2904392.

[4] G. Liang, I. Mudawar, Review of pool boiling enhancement with additives and nanofluids, Int. J. Heat Mass Transfer 124 (2018) 423–453, doi: 10.1016/j.ijheatmasstransfer.2018.03.046.

[5] C.O. Gersey, I. Mudawar, Effects of heater length and orientation on the trigger mechanism for near-saturated flow boiling critical heat flux-II. Critical heat flux model, Int. J. Heat Mass Transfer 38 (4) (1995) 643–654, doi: 10.1016/0017-9310(94)00194-Z.

[6] V.S. Devahdhanush, Y. Lei, Z. Chen, I. Mudawar, Assessing advantages and disadvantages of macro- and micro-channel flow boiling for high-heat-flux thermal management using computational and theoretical/empirical methods, Int. J. Heat Mass Transfer 169 (2021) 120787, doi: 10.1016/j.ijheatmasstransfer.2020.120787.

[7] C. Konishi, I. Mudawar, M.M. Hasan, Investigation of the influence of orientation on critical heat flux for flow boiling with two-phase inlet, Int. J. Heat Mass Transfer 61 (2013) 176–190, doi: 10.1016/j.ijheatmasstransfer.2013.01.076.

[8] S. Mukherjee, I. Mudawar, Pumpless loop for narrow channel and micro-channel boiling, J. Electron. Packag. 125 (3) (2003) 431–441, doi: 10.1115/1.1602708.

[9] G. Liang, I. Mudawar, Review of single-phase and two-phase nanofluid heat transfer in macro-channels and micro-channels, Int. J. Heat Mass Transfer 136 (2019) 324–354, doi: 10.1016/j.ijheatmasstransfer.2019.02.086.

[10] S. Lee, V.S. Devahdhanush, I. Mudawar, Pressure drop characteristics of large length-to-diameter two-phase micro-channel heat sinks, Int. J. Heat Mass Transfer 115 (2017) 1258–1275, doi: 10.1016/j.ijheatmasstransfer.2017.08.104.

[11] M.E. Johns, I. Mudawar, An ultra-high power two-phase jet-impingement avionic clamshell module, J. Electron. Packag. 118 (4) (1996) 264–270, doi: 10.1115/1.2792162.

[12] V.S. Devahdhanush, I. Mudawar, Critical heat flux of confined round single jet and jet array impingement boiling, Int. J. Heat Mass Transfer 169 (2021) 120857, doi: 10.1016/j.ijheatmasstransfer.2020.120857.

[13] K.A. Estes, I. Mudawar, Comparison of two-phase electronic cooling using free jets and sprays, J. Electron. Packag. 117 (4) (1995) 323–332, doi: 10.1115/1.2792112.

[14] F.P. Chiaramonte, J.A. Joshi, Workshop on critical issues in microgravity fluids, transport, and reaction processes in advanced human support technology—Final report, TM-2004-212940, NASA, Washington, DC, USA, 2004.

[15] National Research Council, Recapturing a Future for Space Exploration, The National Academies Press, Washington, DC, USA, 2011, doi: 10.17226/13048.

[16] Y.F. Xue, J.F. Zhao, J.J. Wei, J. Li, D. Guo, S.X. Wan, Experimental study of nucleate pool boiling of FC-72 on smooth surface under microgravity, Microgravity Sci. Technol. 23 (2011) 75–85, doi: 10.1007/s12217-011-9274-5.

[17] M. Misawa, An experimental and analytical investigation of flow boiling heat transfer under microgravity conditions, Ph.D. thesis, University of Florida, FL, USA, 1993.

[18] C. Konishi, H. Lee, I. Mudawar, M.M. Hasan, H.K. Nahra, N.R. Hall, J.D. Wagner, R.L. May, J.R. Mackey, Flow boiling in microgravity: Part 1 – Interfacial behavior and experimental heat transfer results, Int. J. Heat Mass Transfer 81 (2015) 705–720, doi: 10.1016/j.ijheatmasstransfer.2014.10.049.

[19] C. Konishi, H. Lee, I. Mudawar, M.M. Hasan, H.K. Nahra, N.R. Hall, J.D. Wagner, R.L. May, J.R. Mackey, Flow boiling in microgravity: Part 2 – Critical heat flux interfacial behavior, experimental data, and model, Int. J. Heat Mass Transfer 81 (2015) 721–736, doi: 10.1016/j.ijheatmasstransfer.2014.10.052.

[20] T. Oka, Y. Abe, Y.H. Mori, A. Nagashima, Pool boiling of n-pentane, CFC-113, and water under reduced gravity: Parabolic flight experiments with a transparent heater, J. Heat Transfer 117 (2) (1995) 408–417, doi: 10.1115/1.2822537.

[21] J. Kim, J.F. Benton, D. Wisniewski, Pool boiling heat transfer on small heaters: Effect of gravity and subcooling, Int. J. Heat Mass Transfer 45 (19) (2002) 3919–3932, doi: 10.1016/S0017-9310(02)00108-4.

[22] A. Weinzierl, J. Straub, Nucleate pool boiling in microgravity environment, in: Proc. Int. Heat Transfer Conf. 7, Begell House Inc., Munich, Germany, 1982, pp. 21–27, doi: 10.1615/IHTC7.3730.

[23] V.K. Dhir, G.R. Warrier, E. Aktinol, D. Chao, J. Eggers, W. Sheredy, W. Booth, Nucleate pool boiling experiments (NPBX) on the International Space Station, Microgravity Sci. Technol. 24 (5) (2012) 307–325, doi: 10.1007/s12217-012-9315-8.

[24] J. Straub, Boiling heat transfer and bubble dynamics in microgravity, Adv. Heat Transfer 35 (2001) 57–172, doi: 10.1016/S0065-2717(01)80020-4.

[25] H. Merte, Momentum effects in steady nucleate pool boiling during microgravity, Ann. N. Y. Acad. Sci. 1027 (2004) 196–216, doi: 10.1196/annals.1324.018.

[26] C. Colin, J. Fabre, A.E. Dukler, Gas-liquid flow at microgravity conditions—I. Dispersed bubble and slug flow, Int. J. Multiphase Flow 17 (4) (1991) 533–544, doi: 10.1016/0301-9322(91)90048-8.

[27] A.E. Dukler, J.A. Fabre, J.B. McQuillen, R. Vernon, Gas-liquid flow at microgravity conditions: Flow patterns and their transitions, Int. J. Multiphase Flow 14 (4) (1988) 389–400, doi: 10.1016/0301-9322(88)90017-1.

[28] M. Saito, N. Yamaoka, K. Miyazaki, M. Kinoshita, Y. Abe, Boiling two-phase flow under microgravity, Nucl. Eng. Des. 146 (1–3) (1994) 451–461, doi: 10.1016/0029-5493(94)90350-6.

[29] H. Ohta, Experiments on microgravity boiling heat transfer by using transparent heaters, Nucl. Eng. Des. 175 (1–2) (1997) 167–180, doi: 10.1016/S0029-5493(97)00172-6.

[30] C. Baltis, G.P. Celata, M. Cumo, L. Saraceno, G. Zummo, Gravity influence on heat transfer

rate in flow boiling, Microgravity Sci. Technol. 24 (3) (2012) 203–213, doi: 10.1007/s12217-012-9298-5.

[31] S. Luciani, D. Brutin, C. Le Niliot, O. Rahli, L. Tadrist, Flow boiling in minichannels under normal, hyper-, and microgravity: Local heat transfer analysis using inverse methods, J. Heat Transfer 130 (10) (2008) 1–13, doi: 10.1115/1.2953306.

[32] S. Luciani, D. Brutin, C. Le Niliot, L. Tadrist, O. Rahli, Boiling heat transfer in a vertical microchannel: Local estimation during flow boiling with a non intrusive method, Multiphase Sci. Technol. 21 (4) (2009) 297–328, doi: 10.1615/MultScienTechn.v21.i4.30.

[33] H. Ohta, H. Asano, O. Kawanami, K. Suzuki, R. Imai, Y. Shinmoto, S. Matsumoto, T. Kurimoto, H. Takaoka, K. Fujii, M. Sakamoto, K. Sawada, H. Kawasaki, A. Okamoto, K. Kogure, T. Oka, K. Usuku, T. Tomobe, M. Takayanagi, Development of boiling and two-phase flow experiments on board ISS (Research objectives and concept of experimental setup), Int. J. Microgravity Sci. Appl. 33 (1) (2016) 330101, doi: 10.15011/ijmsa.33.330102.

[34] K. Inoue, H. Ohta, Y. Toyoshima, H. Asano, O. Kawanami, R. Imai, K. Suzuki, Y. Shinmoto, S. Matsumoto, Heat loss analysis of flow boiling experiments onboard International Space Station with unclear thermal environmental conditions (1st Report: Subcooled liquid flow conditions at test section inlet), Microgravity Sci. Technol. 33 (2) (2021) 28, doi: 10.1007/s12217-021-09869-5.

[35] K. Inoue, H. Ohta, H. Asano, O. Kawanami, R. Imai, K. Suzuki, Y. Shinmoto, T. Kurimoto, S. Matsumoto, Heat loss analysis of flow boiling experiments onboard International Space Station with unclear thermal environmental conditions (2nd Report: Liquid-vapor two-phase flow conditions at test section inlet), Microgravity Sci. Technol. 33 (5) (2021) 57, doi: 10.1007/s12217-021-09902-7.

[36] H. Zhang, I. Mudawar, M.M. Hasan, Assessment of dimensionless CHF correlations for subcooled flow boiling in microgravity and Earth gravity, Int. J. Heat Mass Transfer 50 (23–24) (2007) 4568–4580, doi: 10.1016/j.ijheatmasstransfer.2007.03.030.

[37] H. Zhang, I. Mudawar, M.M. Hasan, CHF model for subcooled flow boiling in Earth gravity and microgravity, Int. J. Heat Mass Transfer 50 (19–20) (2007) 4039–4051, doi: 10.1016/j.ijheatmasstransfer.2007.01.029.

[38] H. Zhang, I. Mudawar, M.M. Hasan, Experimental and theoretical study of orientation effects on flow boiling CHF, Int. J. Heat Mass Transfer 45 (22) (2002) 4463–4477, doi: 10.1016/S0017-9310(02)00152-7.

[39] C.R. Kharangate, L.E. O'Neill, I. Mudawar, M.M. Hasan, H.K. Nahra, R. Balasubramaniam, N.R. Hall, A.M. Macner, J.R. Mackey, Flow boiling and critical heat flux in horizontal channel with one-sided and double-sided heating, Int. J. Heat Mass Transfer 90 (2015) 323–338, doi: 10.1016/j.ijheatmasstransfer.2015.06.073.

[40] V.S. Devahdhanush, S. Lee, I. Mudawar, Experimental investigation of subcooled flow boiling in annuli with reference to thermal management of ultra-fast electric vehicle charging cables, Int. J. Heat Mass Transfer 172 (2021) 121176, doi: 10.1016/j.ijheatmasstransfer.2021.121176.

[41] V.S. Devahdhanush, S. Lee, I. Mudawar, Consolidated theoretical/empirical predictive method for subcooled flow boiling in annuli with reference to thermal management of ultra-fast electric vehicle charging cables, Int. J. Heat Mass Transfer 175 (2021) 121224, doi: 10.1016/j.ijheatmasstransfer.2021.121224.

[42] S. Lee, V.S. Devahdhanush, I. Mudawar, Investigation of subcooled and saturated boiling heat transfer mechanisms, instabilities, and transient flow regime maps for large length-to-diameter ratio micro-channel heat sinks, Int. J. Heat Mass Transfer 123 (2018) 172–191, doi: 10.1016/j.ijheatmasstransfer.2018.02.020.

[43] P. Saha, N. Zuber, Point of net vapor generation and vapor void fraction in subcooled boiling, in: Proc. Int. Heat Transfer Conf. 5, Begell House Inc., Tokyo, Japan, 1974, pp. 175–179, doi: 10.1615/IHTC5.430.

[44] C. Konishi, I. Mudawar, M.M. Hasan, Criteria for negating the influence of gravity on flow boiling critical heat flux with two-phase inlet conditions, Int. J. Heat Mass Transfer 65 (2013) 203–218, doi: 10.1016/j.ijheatmasstransfer.2013.05.070.

[45] C.R. Kharangate, I. Mudawar, M.M. Hasan, Experimental and theoretical study of critical heat flux in vertical upflow with inlet vapor void, Int. J. Heat Mass Transfer 55 (1–3) (2012) 360–374, doi: 10.1016/j.ijheatmasstransfer.2011.09.028.

[46] C.R. Kharangate, L.E. O'Neill, I. Mudawar, M.M. Hasan, H.K. Nahra, R. Balasubramaniam, N.R. Hall, A.M. Macner, J.R. Mackey, Effects of subcooling and two-phase inlet on flow boiling heat transfer and critical heat flux in a horizontal channel with one-sided and double-sided heating, Int. J. Heat Mass Transfer 91 (2015) 1187–1205, doi: 10.1016/j.ijheatmasstransfer.2015.08.059.

[47] C.R. Kharangate, L.E. O'Neill, I. Mudawar, Effects of two-phase inlet quality, mass velocity, flow orientation, and heating perimeter on flow boiling in a rectangular channel: Part 2 – CHF experimental results and model, Int. J. Heat Mass Transfer 103 (2016) 1280–1296, doi: 10.1016/j.ijheatmasstransfer.2016.05.059.

[48] C.R. Kharangate, L.E. O'Neill, I. Mudawar, L.E. O'Neill, I. Mudawar, L.E. O'Neill, I. Mudawar, Effects of two-phase inlet quality, mass velocity, flow orientation, and heating perimeter on flow boiling in a rectangular channel: Part 1 – Two-phase flow and heat transfer results, Int. J. Heat Mass Transfer 103 (2016) 1261–1279, doi: 10.1016/j.ijheatmasstransfer.2016.05.060.

[49] H. Zhang, I. Mudawar, M.M. Hasan, Flow boiling CHF in microgravity, Int. J. Heat Mass Transfer 48 (15) (2005) 3107–3118, doi: 10.1016/j.ijheatmasstransfer.2005.02.015.

[50] H.K. Nahra, M.M. Hasan, M. Guzik, R. Balasubramaniam, J.R. Mackey, Flow boiling and condensation experiment (FBCE): Capabilities and system description, NASA/TM-20205007641, NASA Glenn Research Center, Cleveland, OH, USA, 2020.

[51] S.J. Darges, V.S. Devahdhanush, I. Mudawar, H.K. Nahra, R. Balasubramaniam, M.M. Hasan, J.R. Mackey, Experimental results and interfacial lift-off model predictions of critical heat flux for flow boiling with subcooled inlet conditions – In preparation for experiments onboard the International Space Station, Int. J. Heat Mass Transfer 183 (2022) 122241, doi: 10.1016/j.ijheatmasstransfer.2021.122241.

[52] S. Lee, V.S. Devahdhanush, I. Mudawar, Experimental and analytical investigation of flow loop induced instabilities in micro-channel heat sinks, Int. J. Heat Mass Transfer 140 (2019) 303–330, doi: 10.1016/j.ijheatmasstransfer.2019.05.077.

[53] L.E. O'Neill, I. Mudawar, Review of two-phase flow instabilities in macro- and micro-channel systems, Int. J. Heat Mass Transfer 157 (2020) 119738, doi: 10.1016/j.ijheatmasstransfer.2020.119738.

[54] J. Lee, I. Mudawar, M.M. Hasan, H.K. Nahra, J.R. Mackey, Experimental and computational investigation of flow boiling in microgravity, Int. J. Heat Mass Transfer 183

(2022) 122237, doi: 10.1016/j.ijheatmasstransfer.2021.122237.

[55] E.W. Lemmon, I.H. Bell, M.L. Huber, M.O. McLinden, NIST Standard Reference Database 23: Reference Fluid Thermodynamic and Transport Properties-REFPROP, Version 10, NIST, Gaithersburg, MD, USA, 2018.

[56] C. Konishi, I. Mudawar, M.M. Hasan, Investigation of localized dryout versus CHF in saturated flow boiling, Int. J. Heat Mass Transfer 67 (2013) 131–146, doi: 10.1016/j.ijheatmasstransfer.2013.07.082.

[57] P.A. Kew, K. Cornwell, Correlations for the prediction of boiling heat transfer in small-diameter channels, Appl. Therm. Eng. 17 (8–10) (1997) 705–715, doi: 10.1016/S1359-4311(96)00071-3.

[58] N. Brauner, A. Ullmann, The Prediction of Flow Boiling Maps in Minichannels, 4th Japanese-European Two-Phase Flow Group Meeting, Kyoto, Japan, 2006.

[59] J.M. Li, B.X. Wang, Size effect on two-phase regime for condensation in micro/mini tubes, Heat Transfer - Asian Res. 32 (1) (2003) 65–71, doi: 10.1002/htj.10076.

[60] C.L. Ong, J.R. Thome, Macro-to-microchannel transition in two-phase flow: Part 1 – Two-phase flow patterns and film thickness measurements, Exp. Therm. Fluid Sci. 35 (1) (2011) 37–47, doi: 10.1016/j.expthermflusci.2010.08.004.

[61] L.E. O'Neill, I. Mudawar, M.M. Hasan, H.K. Nahra, R. Balasubramaniam, J.R. Mackey, Experimental investigation of frequency and amplitude of density wave oscillations in vertical upflow boiling, Int. J. Heat Mass Transfer 125 (2018) 1240–1263, doi: 10.1016/j.ijheatmasstransfer.2018.04.138.

[62] L.E. O'Neill, I. Mudawar, M.M. Hasan, H.K. Nahra, R. Balasubramaniam, N.R. Hall, A. Lokey, J.R. Mackey, Experimental investigation into the impact of density wave oscillations on flow boiling system dynamic behavior and stability, Int. J. Heat Mass Transfer 120 (2018) 144–166, doi: 10.1016/j.ijheatmasstransfer.2017.12.011.

[63] V.S. Devahdhanush, I. Mudawar, Review of critical heat flux (CHF) in jet impingement boiling, Int. J. Heat Mass Transfer 169 (2021) 120893, doi: 10.1016/j.ijheatmasstransfer.2020.120893.

Table 1 Key dimensions of test module (FBM).

Upstream development length, L_d	327.7 mm
Heated length, L_h	114.6 mm
Downstream exit length, L_e	60.7 mm
Thermocouple locations (7) from heated section start, z_{tc}	5.4, 22.7, 40.0, 57.3, 74.6, 91.9, 109.2 mm
Channel height (unheated), H	5.0 mm
Channel width (heated), W	2.5 mm

Table 2 Measurement uncertainties.

Measured Parameters	**Maximum Uncertainty**

Temperature (thermocouples)	±0.5°C
Temperature (RTDs)	±0.5°C
Pressure	±0.7 kPa
FBM heater power	±0.3% reading
Preheater power	±0.6% reading
Mass flow rate	±0.6% full-scale reading

Table 3 Summary of key parameters of MST steady-state database for subcooled inlet.

	Single-sided Heating	**Double-sided Heating**
Mass velocity, G	179.60 – 3199.98 kg/m^{2}s	179.65 – 3200.00 kg/m^{2}s
Mass flow rate, $\dot{m}$	2.25 – 40.00 g/s	2.25 – 40.00 g/s
Inlet pressure, p_{in}	119.02 – 177.17 kPa	118.61 – 190.81 kPa
Inlet temperature, T_{in}	34.01 – 71.63˚C	34.89 – 72.95˚C
Inlet subcooling, $\Delta T_{sub,in}$	+0.00 – 31.77˚C	0.18 – 32.00˚C
Inlet quality, $x_{e,in}$	-0.422 – -0.000	-0.429 – -0.003
Wall heat flux, q''_w	2.07 – 48.09 W/cm^2	1.80 – 49.49 W/cm^2
Outlet pressure, p_{out}	113.18 – 168.04 kPa	113.25 – 172.75 kPa
Outlet temperature, T_{out}	35.90 – 71.41˚C	36.99 – 72.12˚C
Outlet subcooling, $\Delta T_{sub,out}$	0.00 – 26.91˚C	0.00 – 26.04˚C
Outlet quality, $x_{e,out}$	-0.354 – 0.209	-0.342 – 0.460
Local wall temperature, $T_{wa,z}$	56.90 – 117.38°C (heated) 36.26 – 70.97°C (unheated)	58.17 – 115.95°C

Table 4 Summary of key observations from the present MST experiments in Earth gravity.
(a) Differences in various aspects for different heating configurations.

Aspect	**Single-sided Heating**	**Double-sided Heating**
Evolution of bubble boundary layer and vapor layer	Develops only along the one heated wall and hence no interactions. At higher heat fluxes, the layers are thick enough to fill the entire channel width, especially towards the exit.	Develops along both heated walls and hence interacts with each other after reaching a certain thickness. Particularly at higher flow rates, regular gear-teeth-meshing type wavy interfaces form with the liquid separating the two vapor layers.
Local wall temperature	For similar heat flux percentages, there are no significant differences.	For similar heat flux percentages, there are no significant differences. For some cases, T_w overshoot due to delayed ONB leads to upstream local

		T_w differences between the two heated walls.
Local heat transfer coefficient	For similar heat flux percentages, there are no significant differences.	For similar heat flux percentages, there are no significant differences. For some cases, delayed ONB results in local h differences between the two heated walls upstream.
Average heat transfer coefficient	There are no significant differences in the trends of $\overline{h}$ versus wall heat flux.	There are no significant differences in the trends of $\overline{h}$ versus wall heat flux.
Onset of nucleate boiling degradation and critical heat flux	Manifests at larger heat fluxes than double-sided for low mass velocities with highly subcooled inlet.	Manifests at larger heat fluxes than single-sided for high mass velocities with near-saturated inlet.

(b) Differences in various aspects for different degrees of inlet subcooling.

Aspect	**Highly Subcooled Inlet**	**Near-Saturated Inlet**
Evolution of bubble boundary layer and vapor layer	Both bubble boundary layer and vapor layer are thinner. All vapor structures are smaller at a given streamwise location. Flow regime transitions occur both further downstream and at higher heat fluxes. At low mass velocities and high heat fluxes, slug/churn-like flow is observed only near the channel exit. At high mass velocities and high heat fluxes, the wavy vapor layer is thinner, has fewer crests, and are of longer wavelength.	Both bubble boundary layer and vapor layer are thicker. All vapor structures are larger at a given streamwise location. Flow regime transitions occur both upstream and at lower heat fluxes. At low mass velocities and high heat fluxes, slug/churn-like flow covers most of the channel. At high mass velocities and high heat fluxes, the wavy vapor layer is thicker, has more crests, and are of shorter wavelength.
Local wall temperature	T_w is maximum at a narrow location, a short distance upstream of the exit (location 6 of 7).	T_w is maximum over a wider region from channel middle to just before the exit (locations 4-6 of 7).
Local heat transfer coefficient	Only the downstream part of streamwise h profile is degraded.	The entire streamwise h profile is severely degraded at higher heat fluxes.
Average heat transfer coefficient	$\overline{h}$ versus heat flux shows a more linear and prolonged increase before reaching the peak. For similar wall heat fluxes, $\overline{h}$ is higher. Peak $\overline{h}$ is also higher.	$\overline{h}$ versus heat flux shows a less linear and short increase before reaching the peak. For similar wall heat fluxes, $\overline{h}$ is lower. Peak $\overline{h}$ is also lower.
Onset of nucleate boiling degradation and critical heat flux	Manifests at larger wall heat fluxes.	Manifests at smaller wall heat fluxes.

(c) Differences in various aspects for different mass velocities.

Aspect	**Low Mass Velocity**	**High Mass Velocity**
Evolution of bubble boundary layer and vapor layer	Both bubble boundary layer and vapor layer are thicker. Flow regime transitions occur upstream. Transition to the slug/churn-like flow regime occurs very early; and it occupies most of the channel even at low heat fluxes.	Both bubble boundary layer and vapor layer are thinner. Flow regime transitions occur further downstream. Transition to slug/churn-like flow is rarely seen; sometimes at channel downstream close to CHF. CHF is mainly due to extinguishing of wetting fronts of the wavy interfaces.
Local wall temperature	For similar heat fluxes, T_w is higher all along the channel. But for similar heat flux percentages, no notable differences in $T_{w,z}$ profiles.	For similar heat fluxes, T_w is lower all along the channel. But for similar heat flux percentages, no notable differences in $T_{w,z}$ profiles.
Local heat transfer coefficient	Streamwise h profile degradation is severe at higher heat flux percentages.	Streamwise h profile degradation is not so severe at higher heat flux percentages.
Average heat transfer coefficient	Peak $\overline{h}$ is at smaller heat flux.	Peak $\overline{h}$ is at larger heat flux.
Onset of nucleate boiling degradation and critical heat flux	Manifests at smaller wall heat fluxes.	Manifests at larger wall heat fluxes.

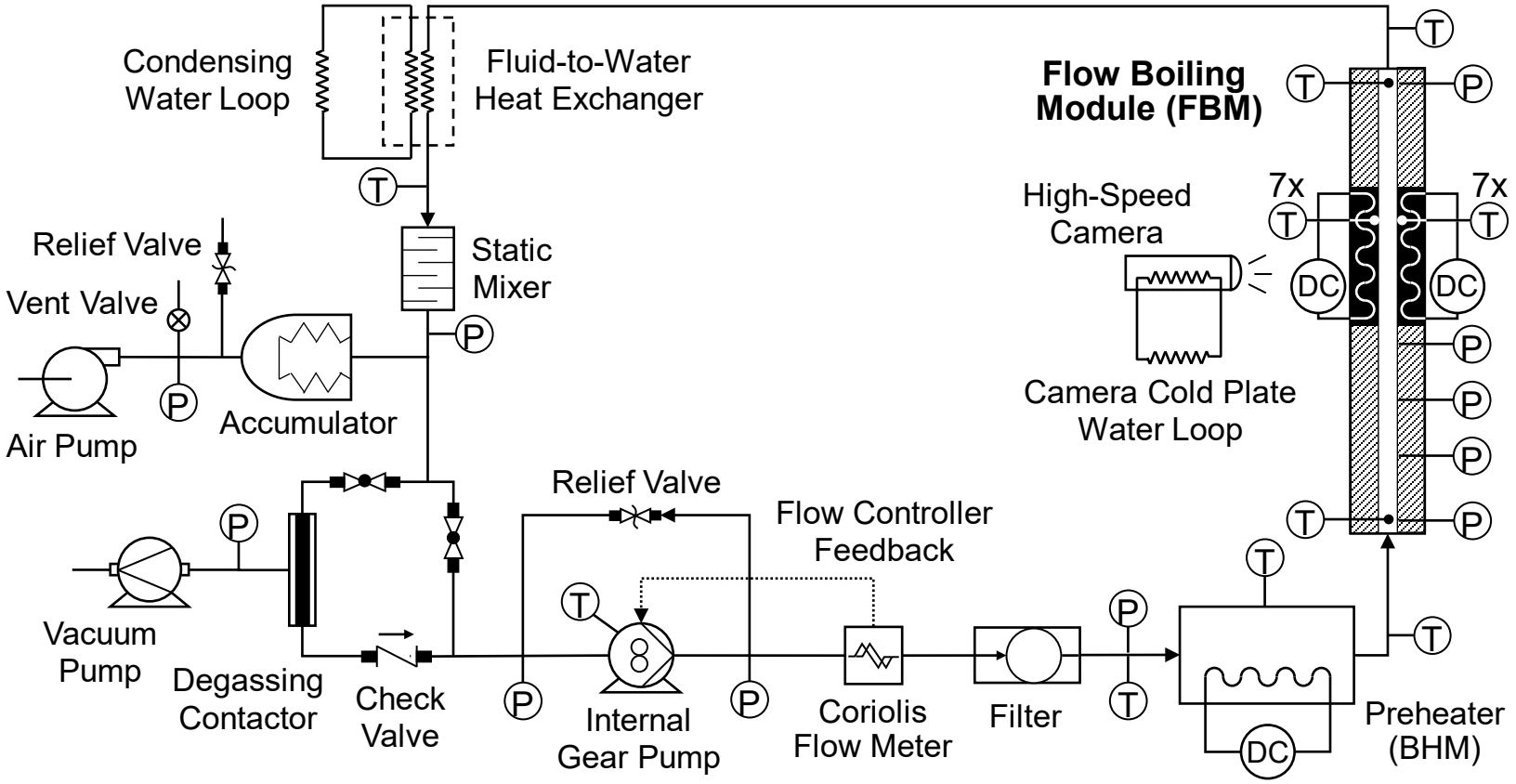

Fig. 1 Schematic diagram of experimental two-phase flow loop.

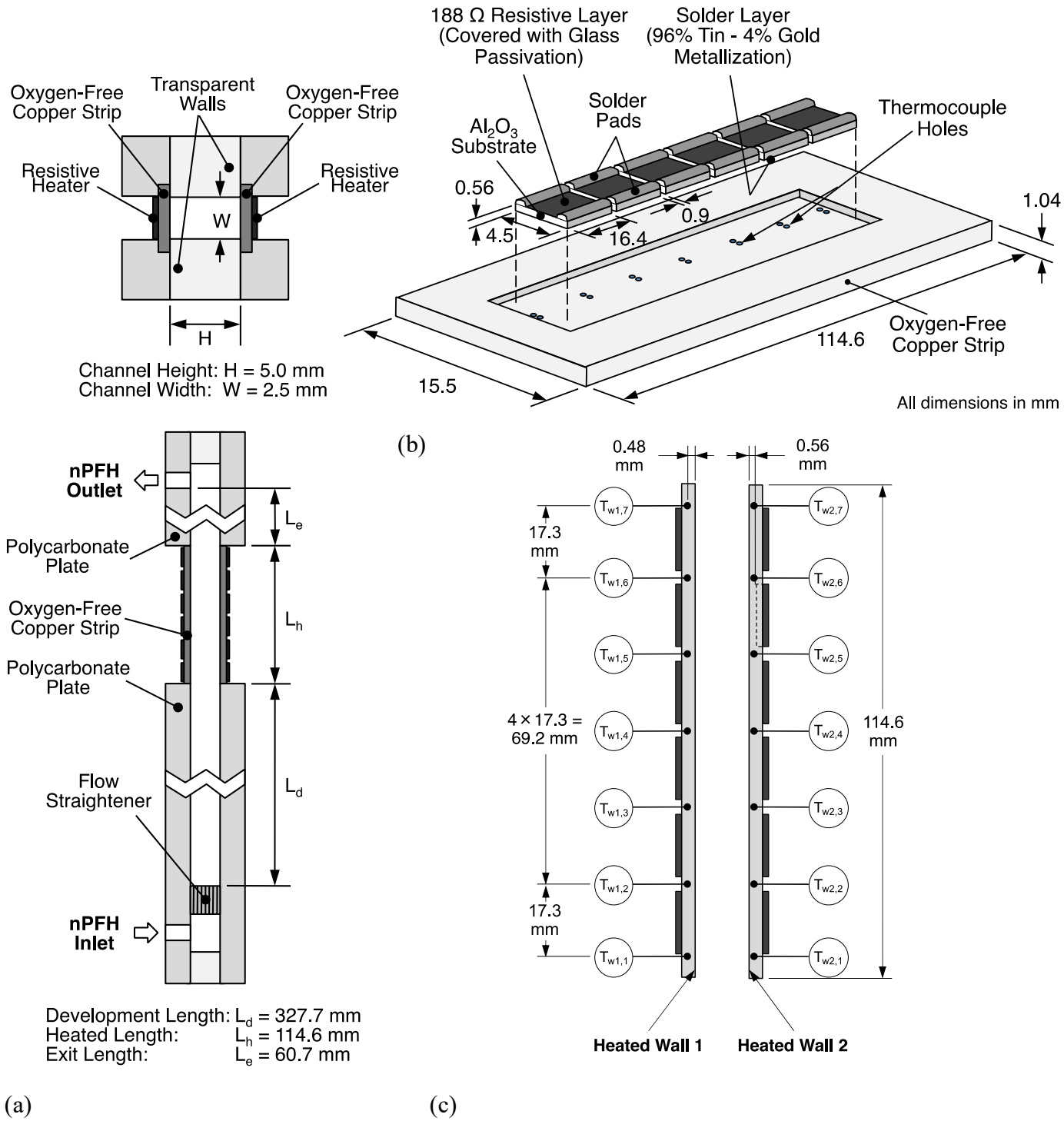

Fig. 2 Schematic representations of (a) overall construction of Flow Boiling Module (FBM), (b) construction of heating strips, and (c) designation of heated walls and local wall temperatures.

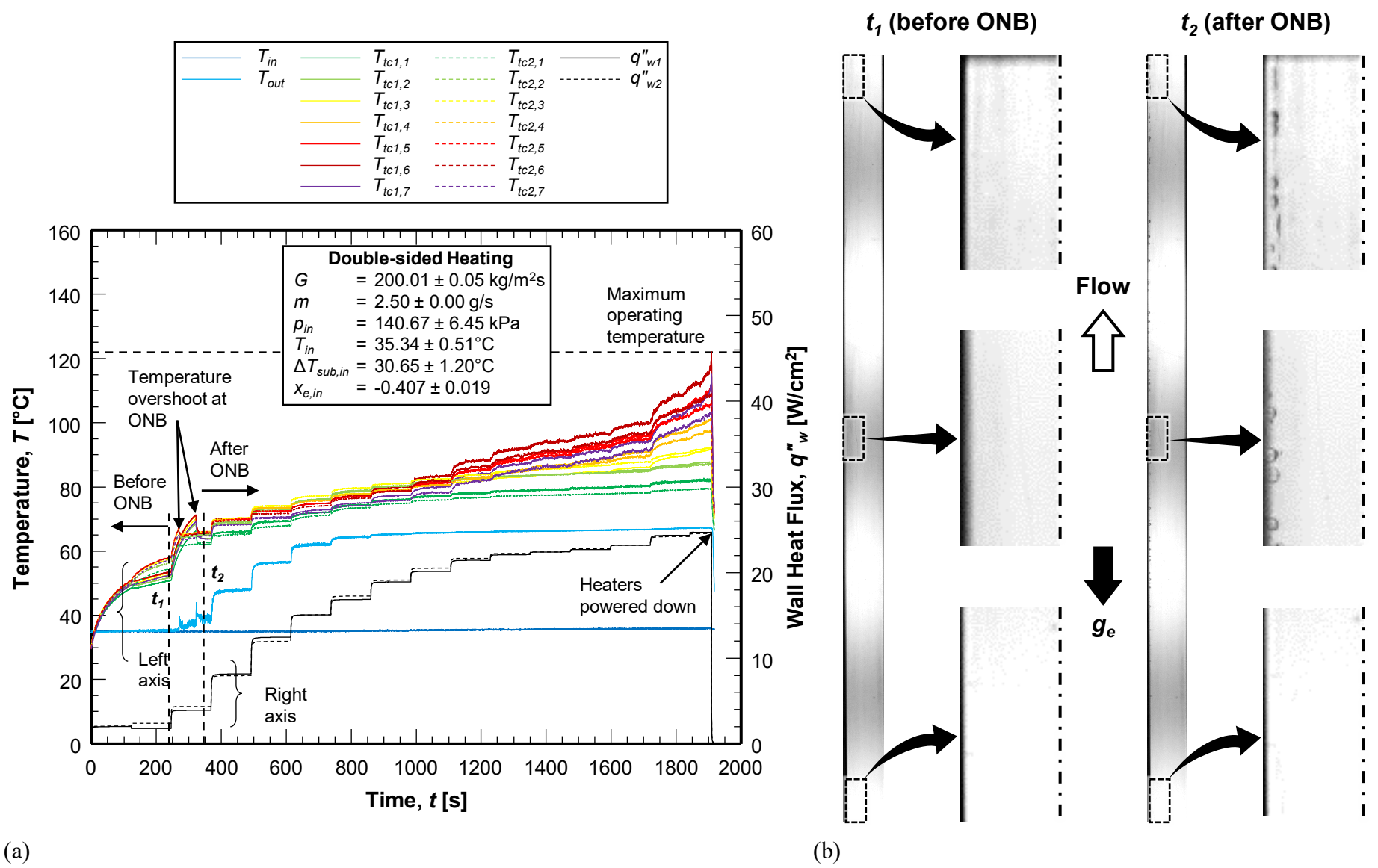

Fig. 3 (a) Temporal variations of fluid inlet, fluid outlet, and heated-strip temperatures for heat flux increments from zero to critical heat flux for a set of operating conditions. (b) Flow visualization at time instants t_1 (steady-state period preceding ONB) and t_2 (steady-state period succeeding ONB).

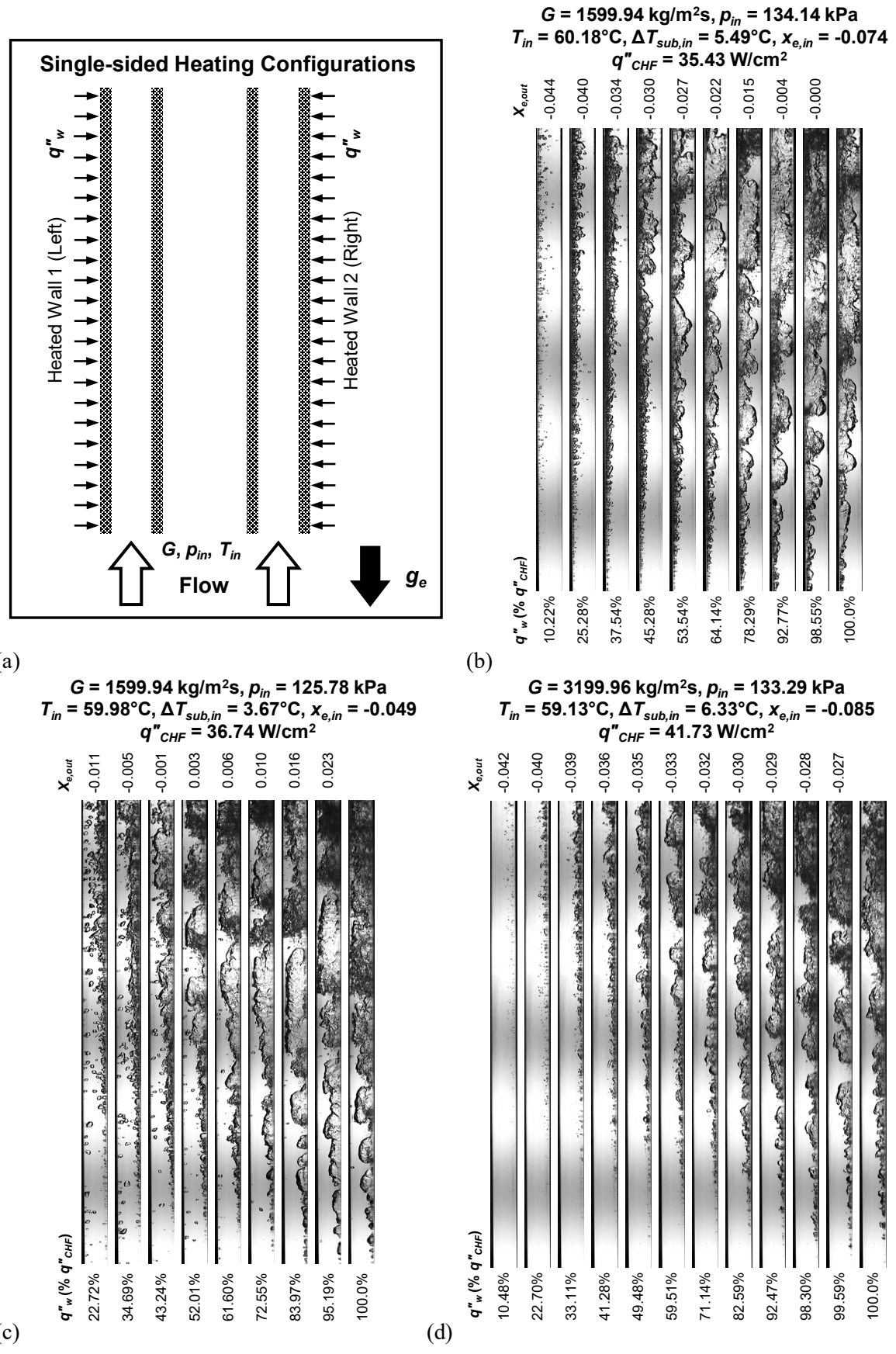

Fig. 4 (a) Schematic representation of single-sided heating configurations. Flow patterns along the boiling curve until CHF for near-saturated inlet at mass velocities of G = (b) 1599.94 (left wall heated), (c) 1599.94 (right wall heated), and (d) 3199.96 kg/m^{2}s (right wall heated).

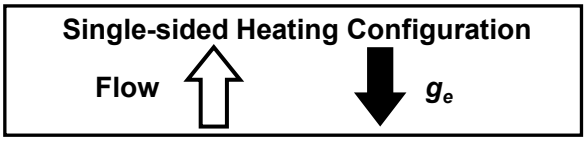

G = 1599.94 kg/m²s, p_{in} = 125.78 kPa, T_{in} = 59.98°C, $\Delta T_{sub,in}$ = 3.67°C, $x_{e,in}$ = -0.049
q''_{CHF} = 36.74 W/cm²

q''_w = 72.55% q''_{CHF}, $x_{e,out}$ = 0.010

q''_w = 95.19% q''_{CHF}, $x_{e,out}$ = 0.023

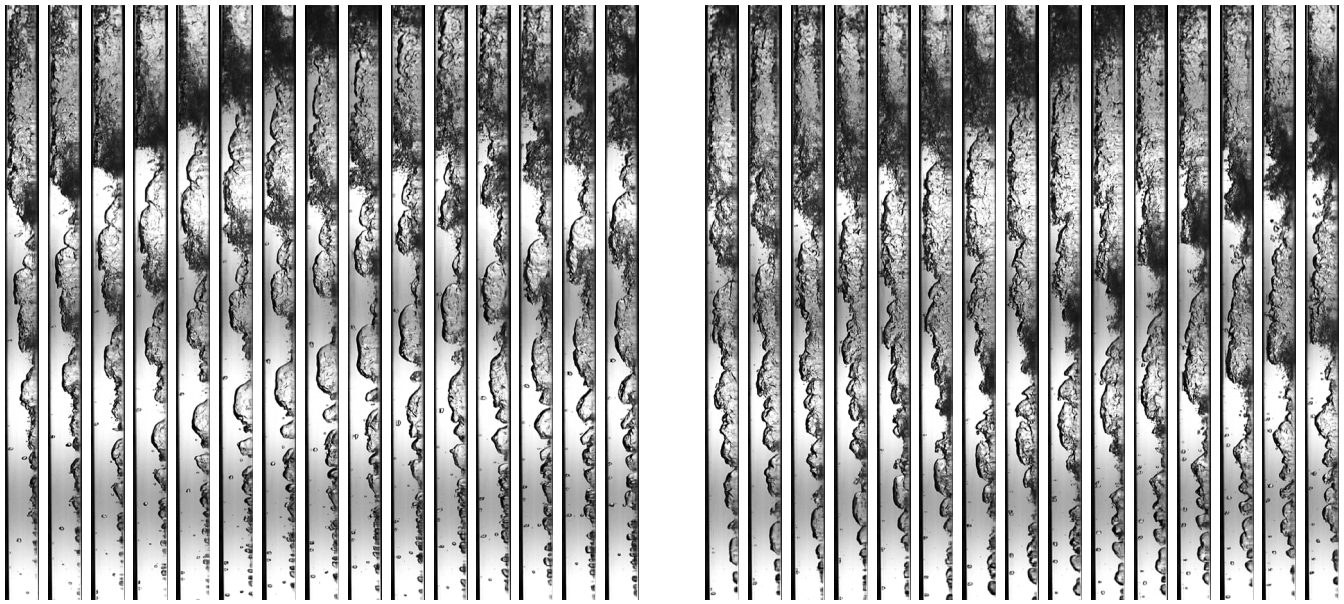

(a)

G = 3199.96 kg/m²s, p_{in} = 133.29 kPa, T_{in} = 59.13°C, $\Delta T_{sub,in}$ = 6.33°C, $x_{e,in}$ = -0.085
q''_{CHF} = 41.73 W/cm²

q''_w = 71.14% q''_{CHF}, $x_{e,out}$ = -0.032

q''_w = 92.47% q''_{CHF}, $x_{e,out}$ = -0.029

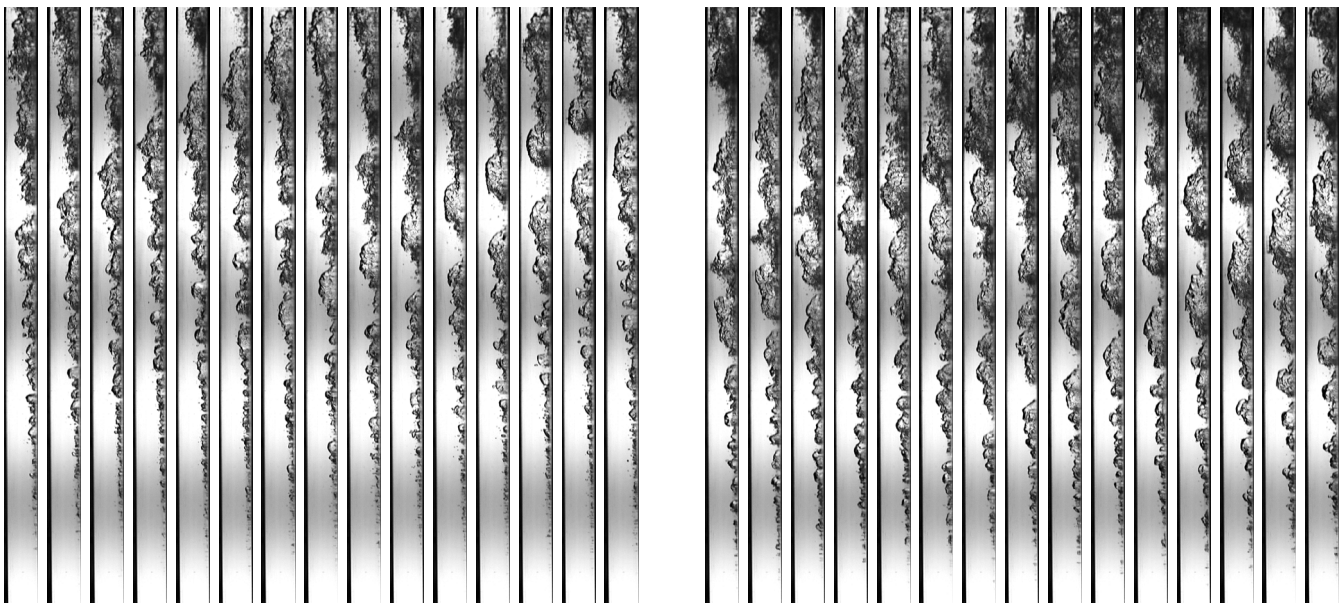

(b)

Fig. 5 Flow visualization image sequences for near-saturated inlet with single-sided heating at mass velocities of G = (a) 1599.94 and (b) 3199.96 kg/m²s. Images in each sequence are 1.5 ms apart.

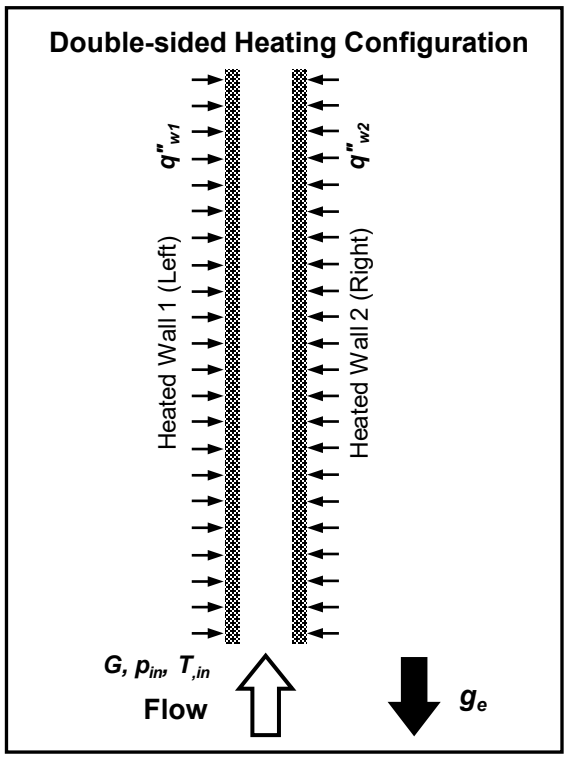

(a)

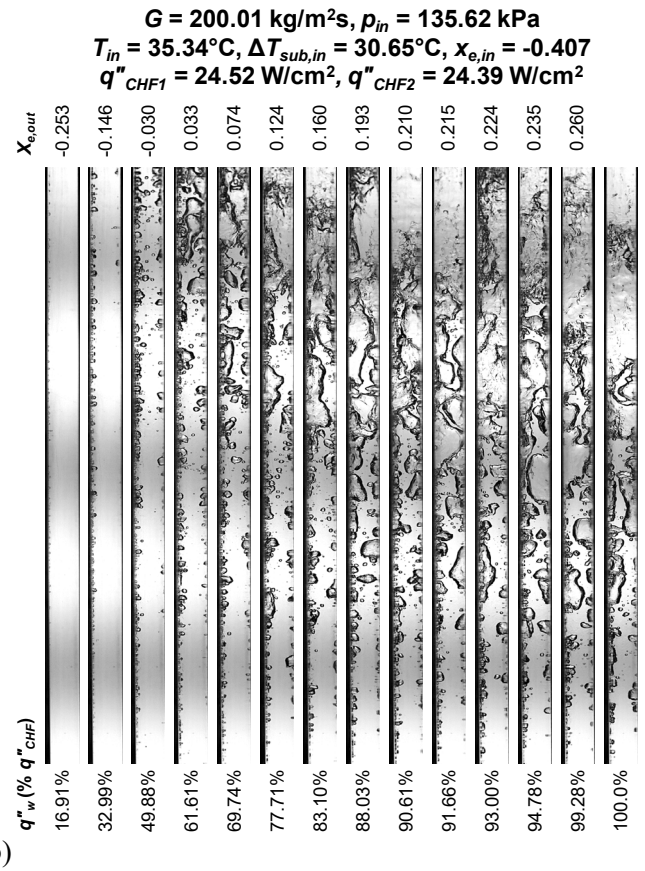

(b)

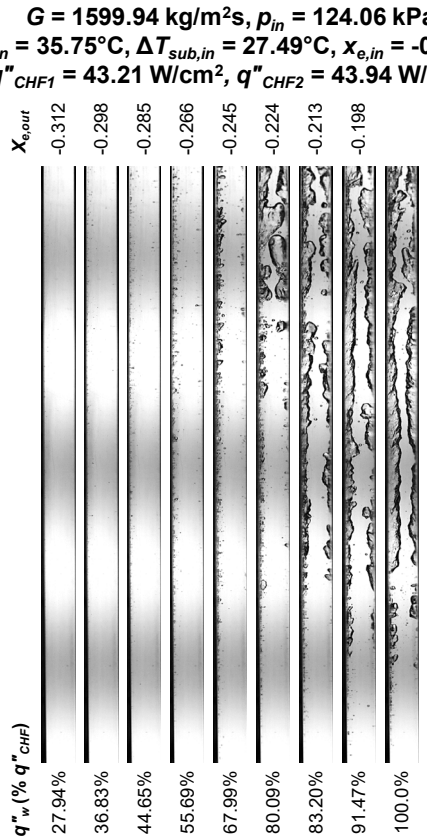

(c)

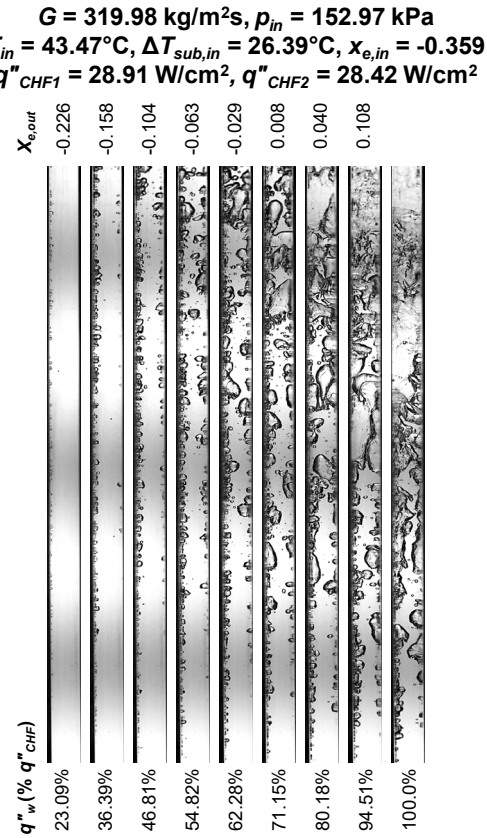

(d)

Fig. 6 (a) Schematic representation of double-sided heating configuration. Flow patterns along the boiling curve until CHF for highly subcooled inlet at mass velocities of G = (b) 200.01, (c) 1599.94, and (d) 319.98 kg/m²s with both walls heated. Note that (d) is at higher inlet pressure.

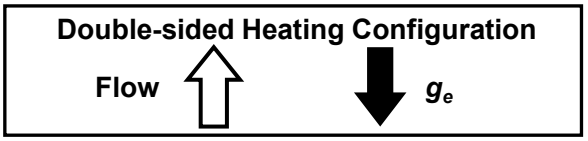

G = 200.01 kg/m²s, p_{in} = 135.62 kPa, T_{in} = 35.34°C, $\Delta T_{sub,in}$ = 30.65°C, $x_{e,in}$ = -0.407
q''_{CHF1} = 24.52 W/cm², q''_{CHF2} = 24.39 W/cm²

q''_w = 69.74% q''_{CHF}, $x_{e,out}$ = 0.074

q''_w = 94.78% q''_{CHF}, $x_{e,out}$ = 0.235

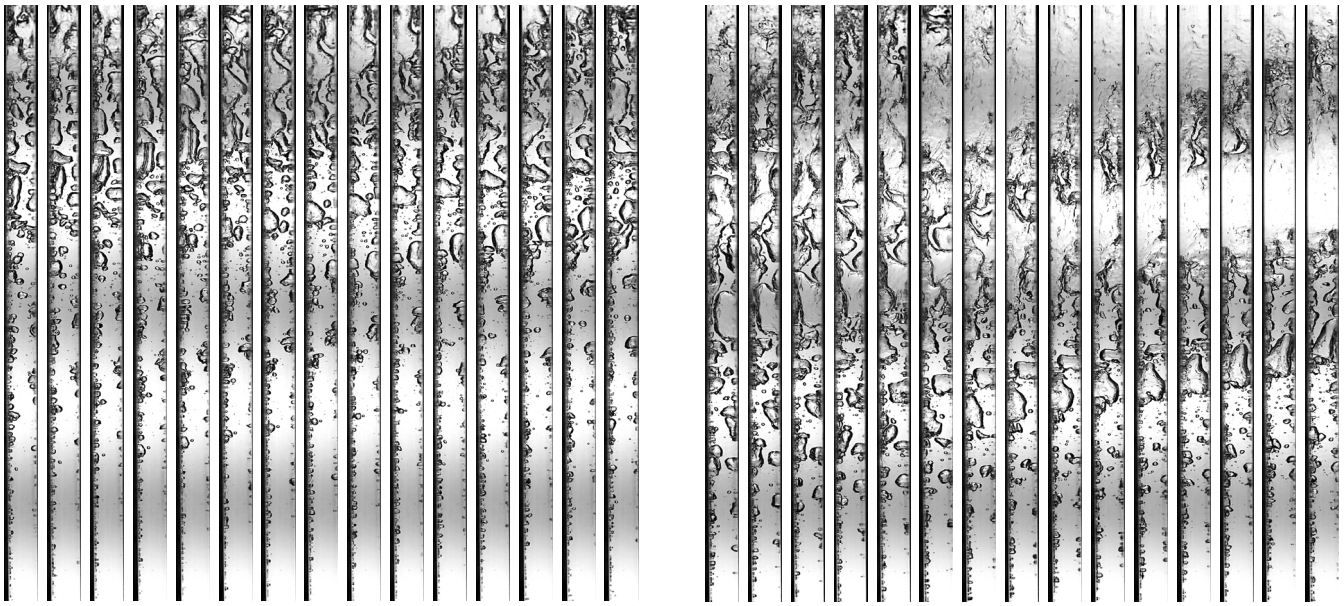

(a)

G = 1599.94 kg/m²s, p_{in} = 124.06 kPa, T_{in} = 35.75°C, $\Delta T_{sub,in}$ = 27.49°C, $x_{e,in}$ = -0.361
q''_{CHF1} = 43.21 W/cm², q''_{CHF2} = 43.94 W/cm²

q''_w = 67.99% q''_{CHF}, $x_{e,out}$ = -0.245

q''_w = 91.47% q''_{CHF}, $x_{e,out}$ = -0.198

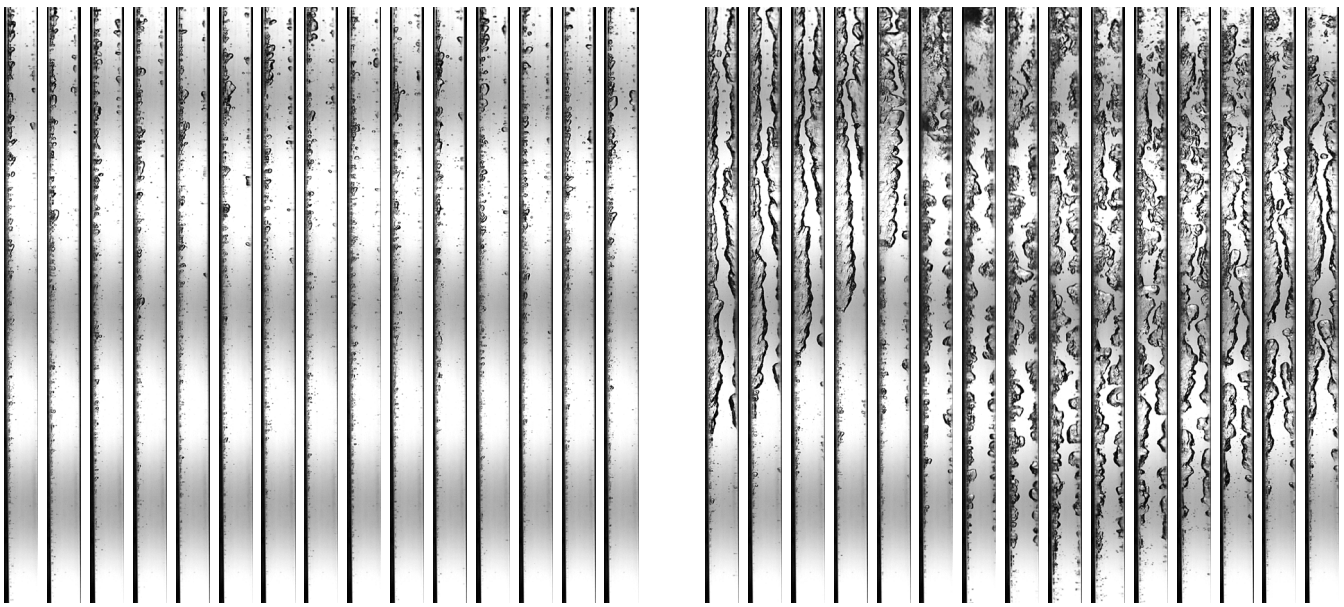

(b)

Fig. 7 Flow visualization image sequences for highly subcooled inlet with double-sided heating at mass velocities of G = (a) 200.01 and (b) 1599.94 kg/m²s. Images in each sequence are 5.0 ms apart.

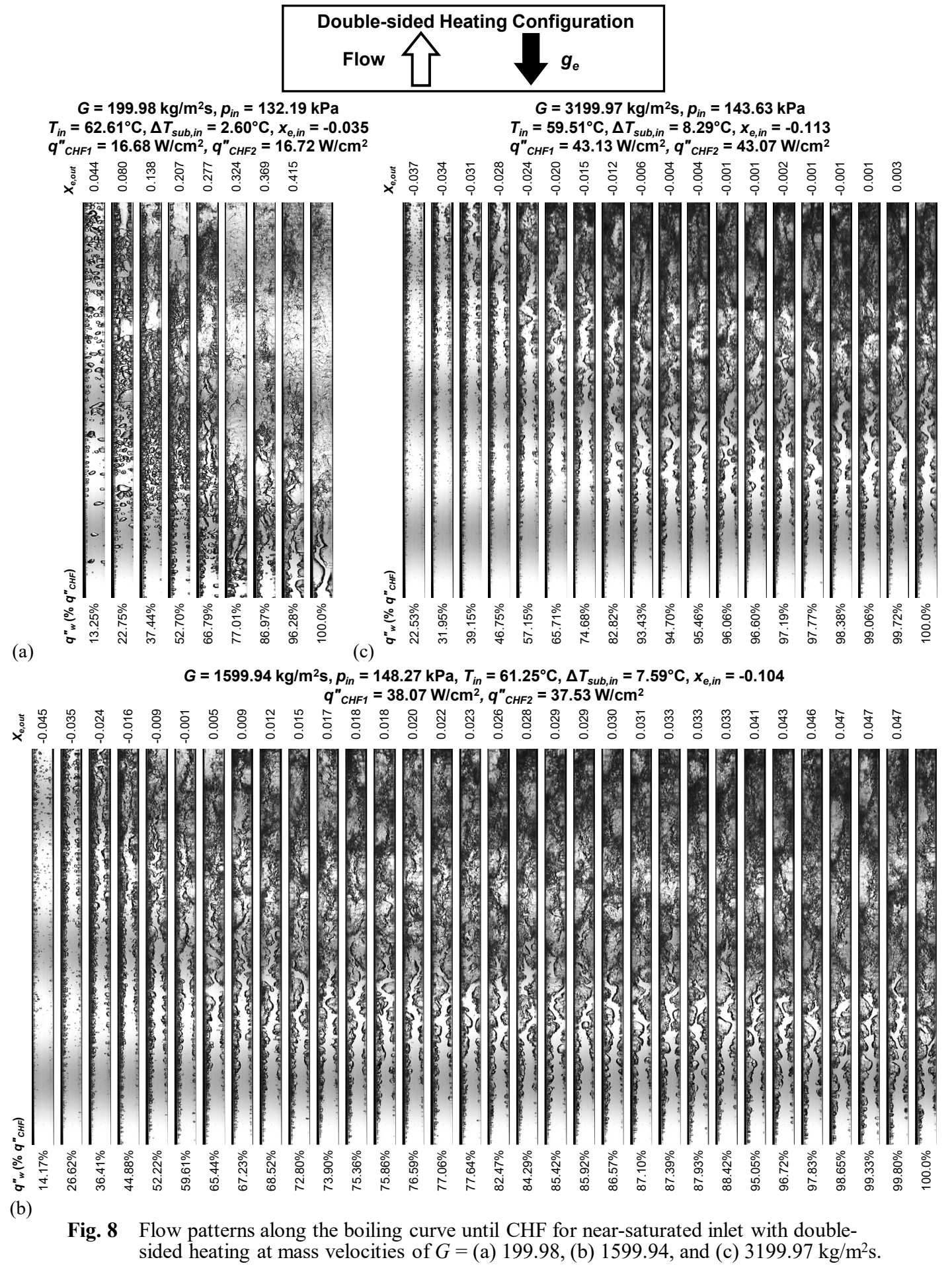

Fig. 8 Flow patterns along the boiling curve until CHF for near-saturated inlet with double-sided heating at mass velocities of G = (a) 199.98, (b) 1599.94, and (c) 3199.97 kg/m²s.

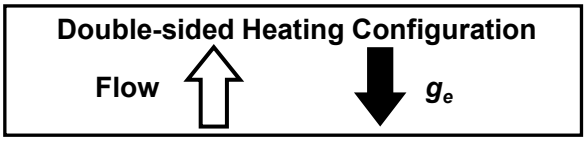

G = 1599.94 kg/m²s, p_{in} = 148.27 kPa, T_{in} = 61.25°C, $\Delta T_{sub,in}$ = 7.59°C, $x_{e,in}$ = -0.104
q''_{CHF1} = 38.07 W/cm², q''_{CHF2} = 37.53 W/cm²

q''_w = 68.52% q''_{CHF}, $x_{e,out}$ = 0.012

q''_w = 95.05% q''_{CHF}, $x_{e,out}$ = 0.041

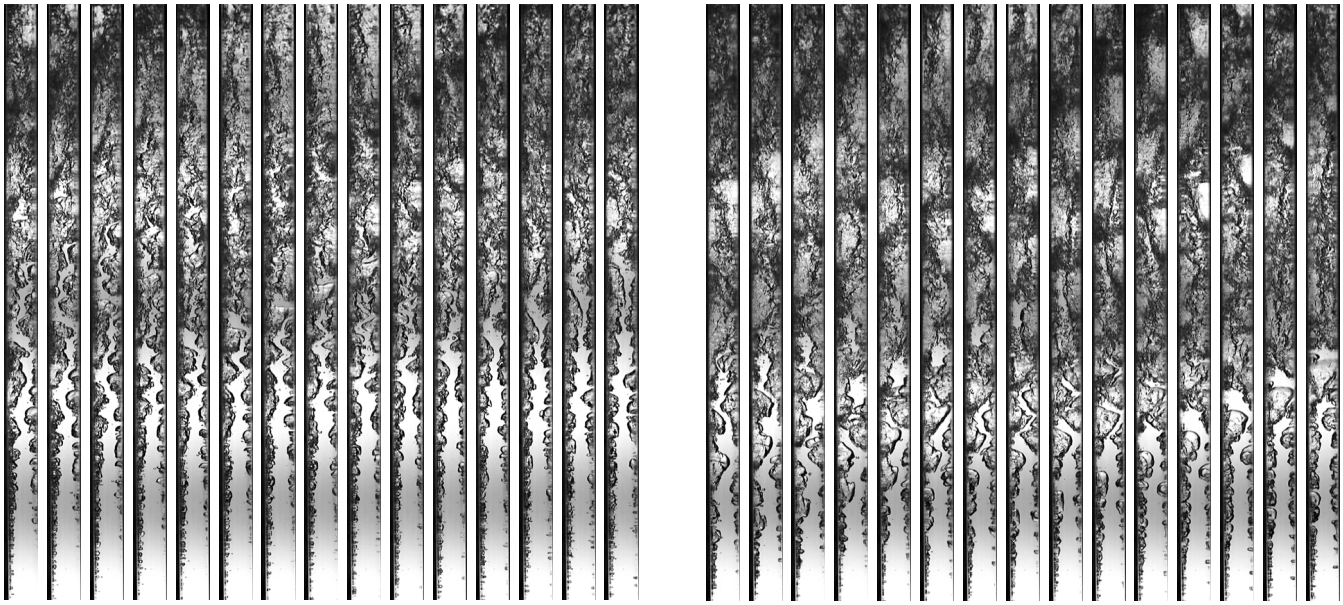

(a)

G = 3199.97 kg/m²s, p_{in} = 143.63 kPa, T_{in} = 59.51°C, $\Delta T_{sub,in}$ = 8.29°C, $x_{e,in}$ = -0.113
q''_{CHF1} = 43.13 W/cm², q''_{CHF2} = 43.07 W/cm²

q''_w = 65.71% q''_{CHF}, $x_{e,out}$ = -0.020

q''_w = 94.70% q''_{CHF}, $x_{e,out}$ = -0.004

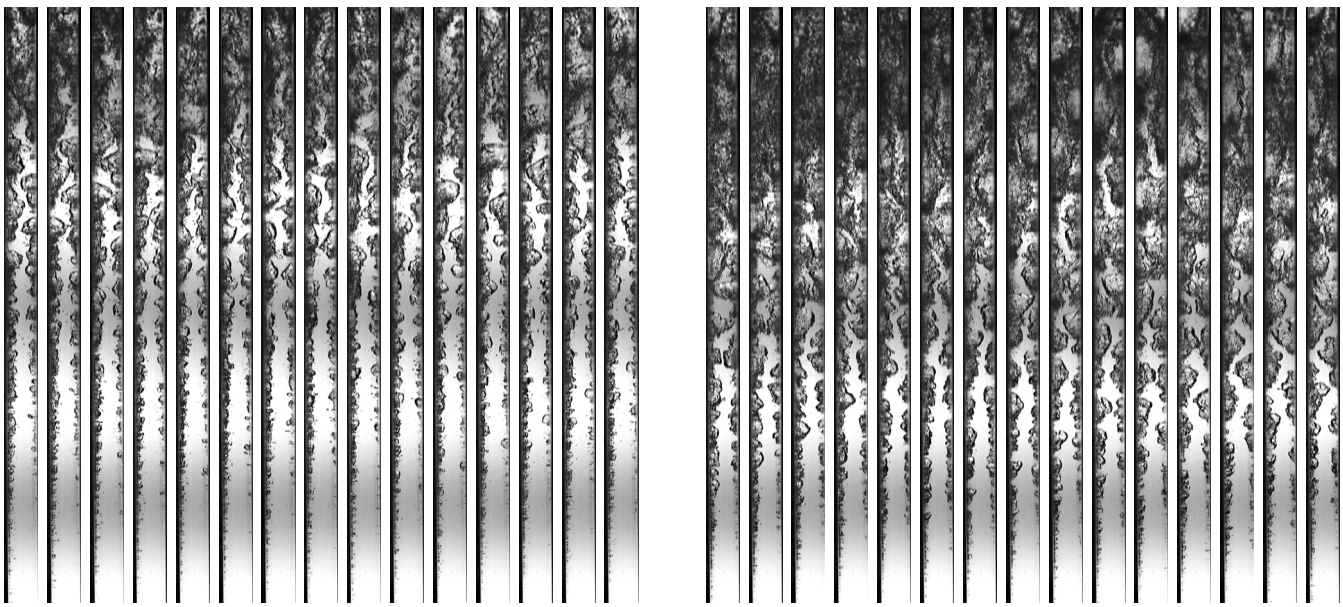

(b)

Fig. 9 Flow visualization image sequences for near-saturated inlet with double-sided heating at mass velocities of G = (a) 1599.94 and (b) 3199.97 kg/m²s. Images in each sequence are 1.5 ms apart.

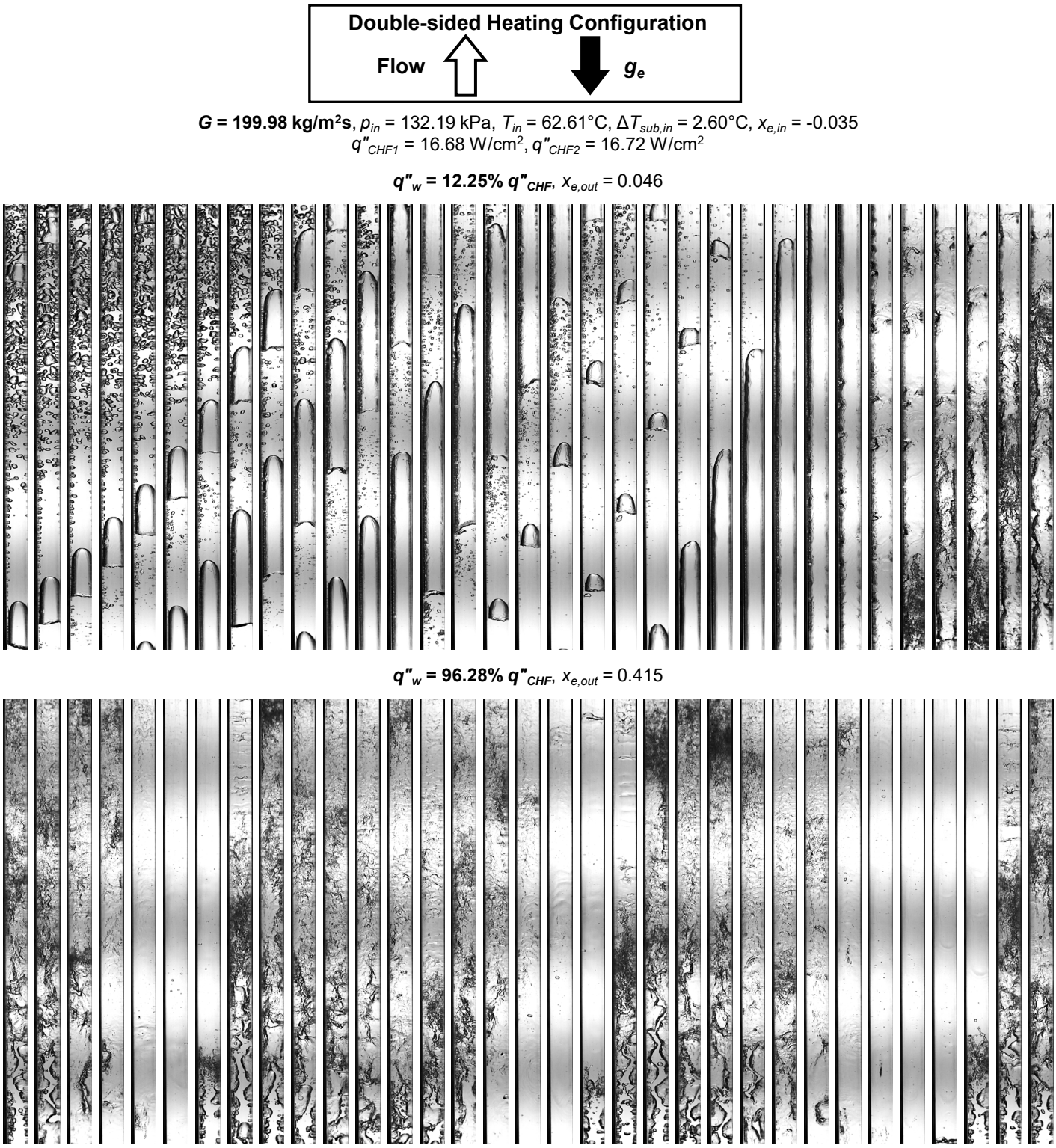

Fig. 10 Flow visualization image sequences for near-saturated inlet with double-sided heating at a mass velocity of G = 199.98 kg/m²s and heat fluxes of q''_w = 12.25% q''_{CHF} and 96.28% q''_{CHF}. Images in each sequence are 25 ms apart.

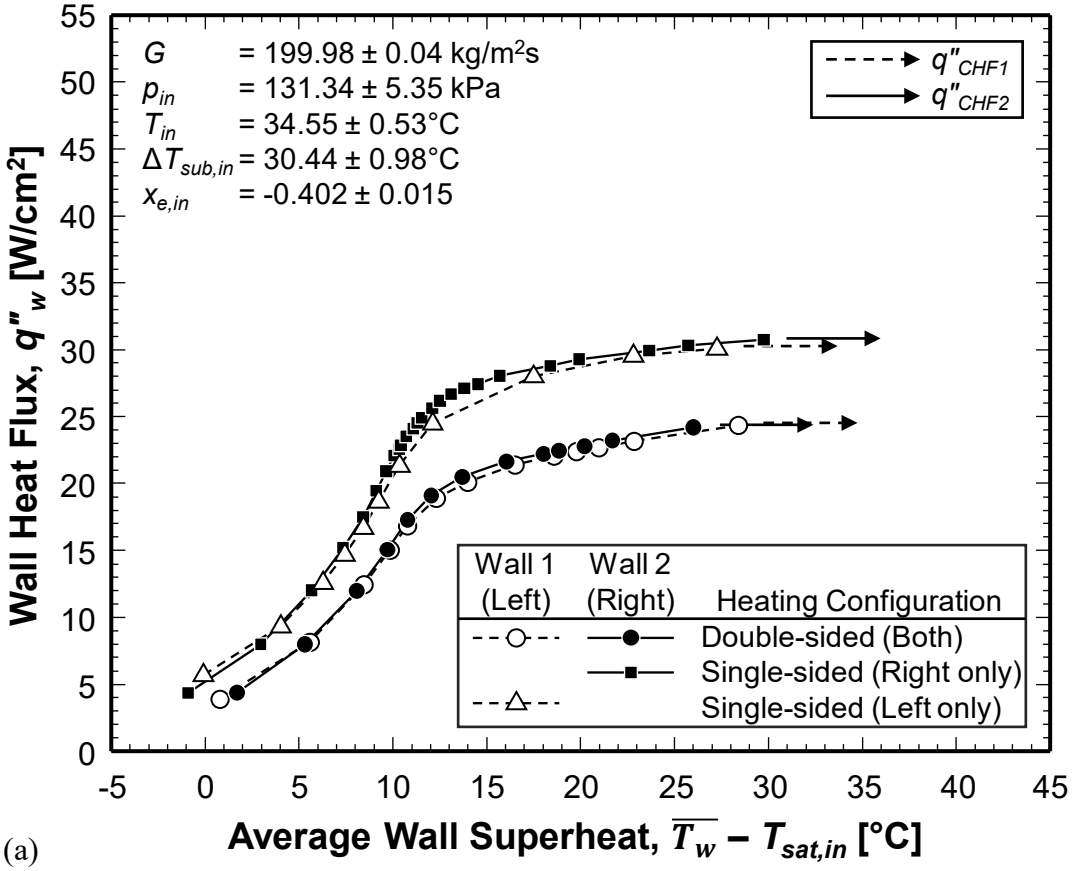

(a)

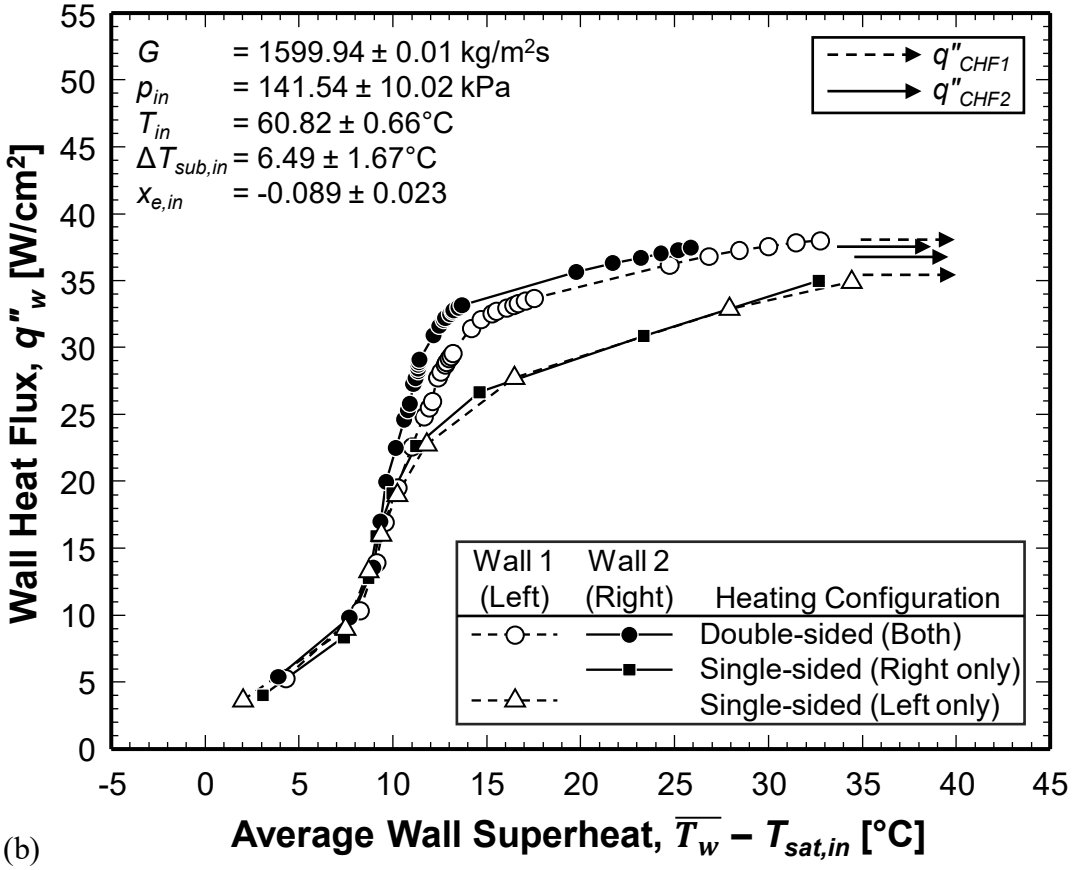

(b)

Fig. 11 Boiling curves illustrating heating configuration effects for (a) low mass velocity with high inlet subcooling and (b) high mass velocity with low inlet subcooling.

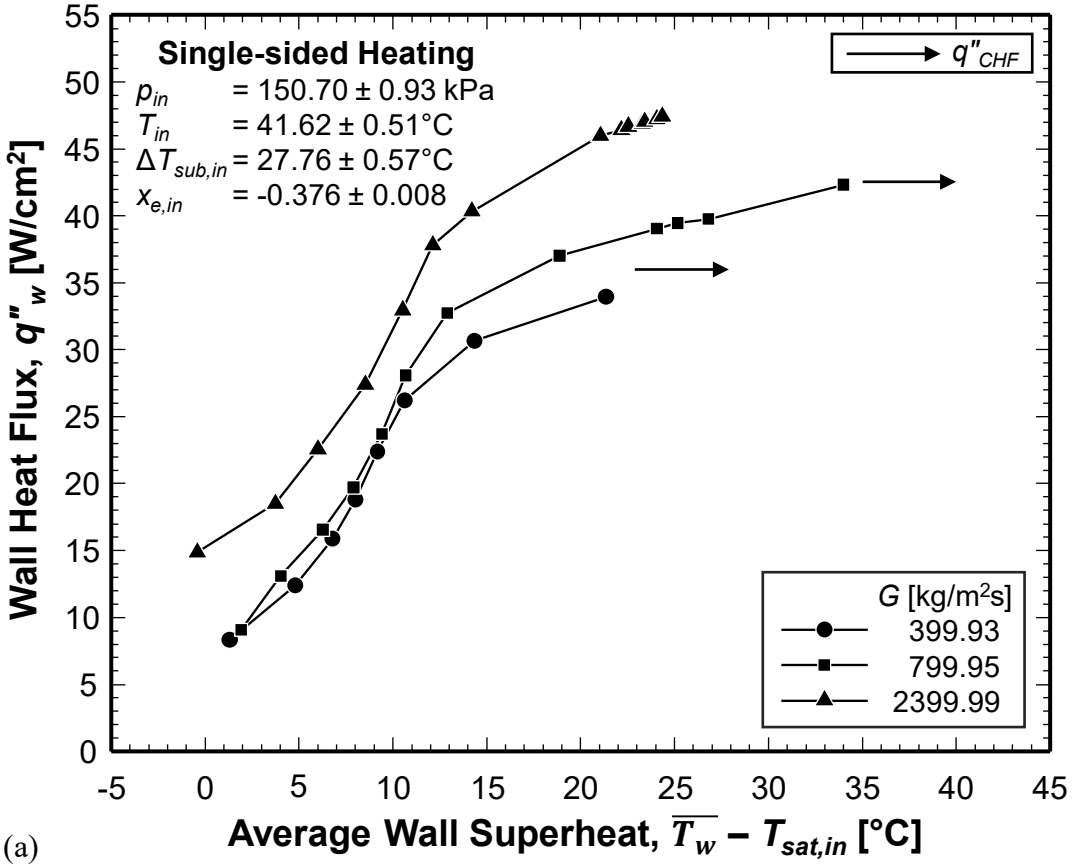

(a)

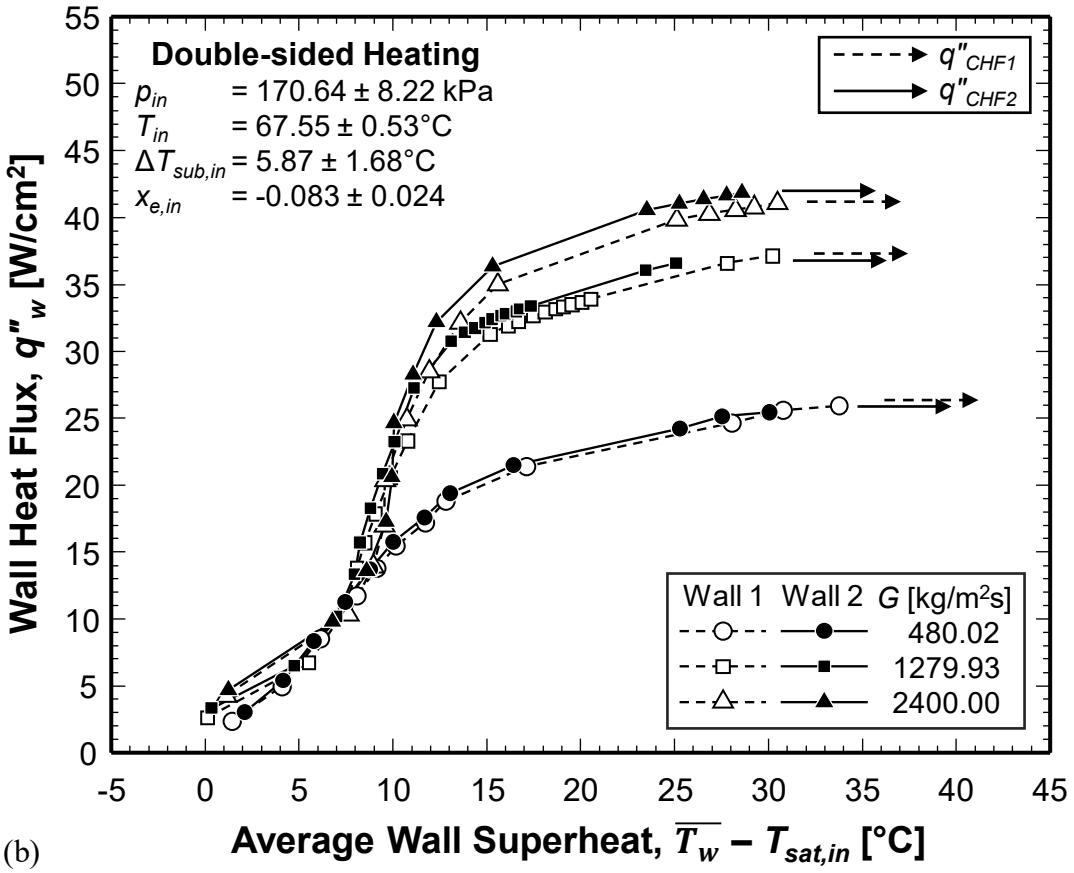

(b)

Fig. 12 Boiling curves illustrating the effects of mass velocity for (a) highly subcooled inlet with single-sided heating and (b) near saturated inlet with double-sided heating.

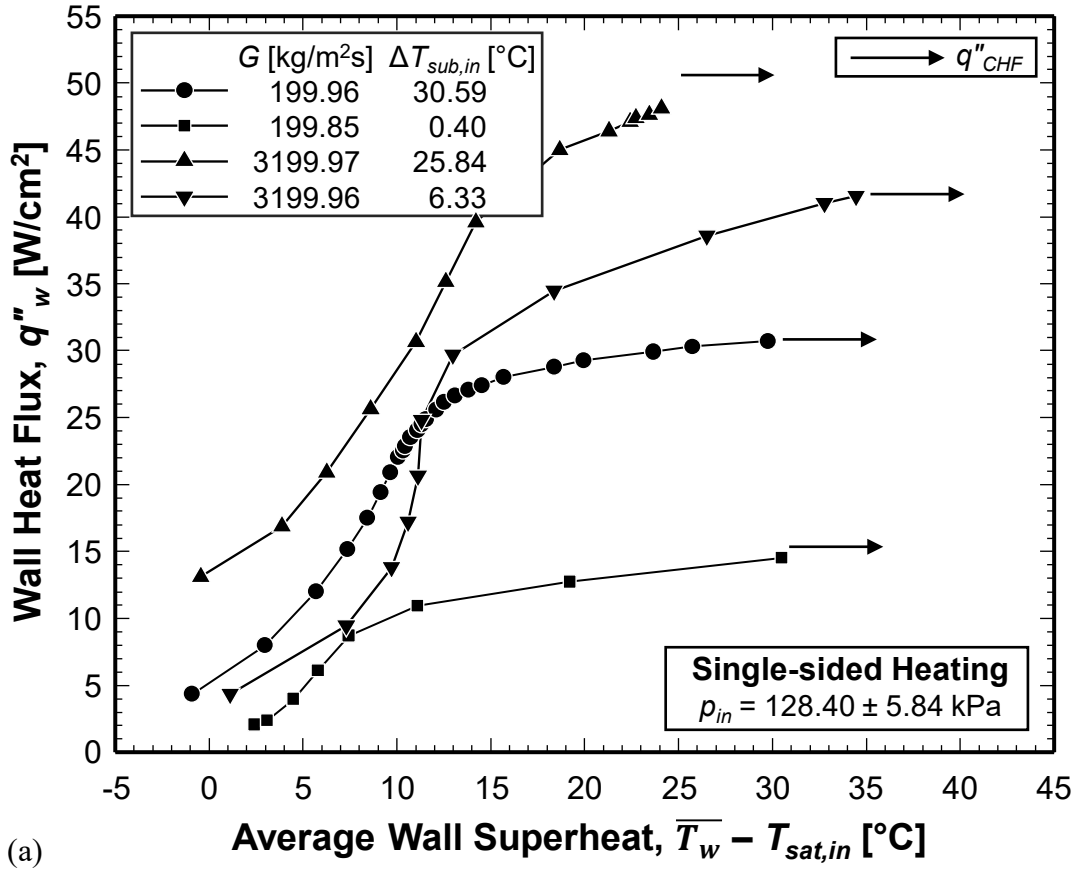

(a)

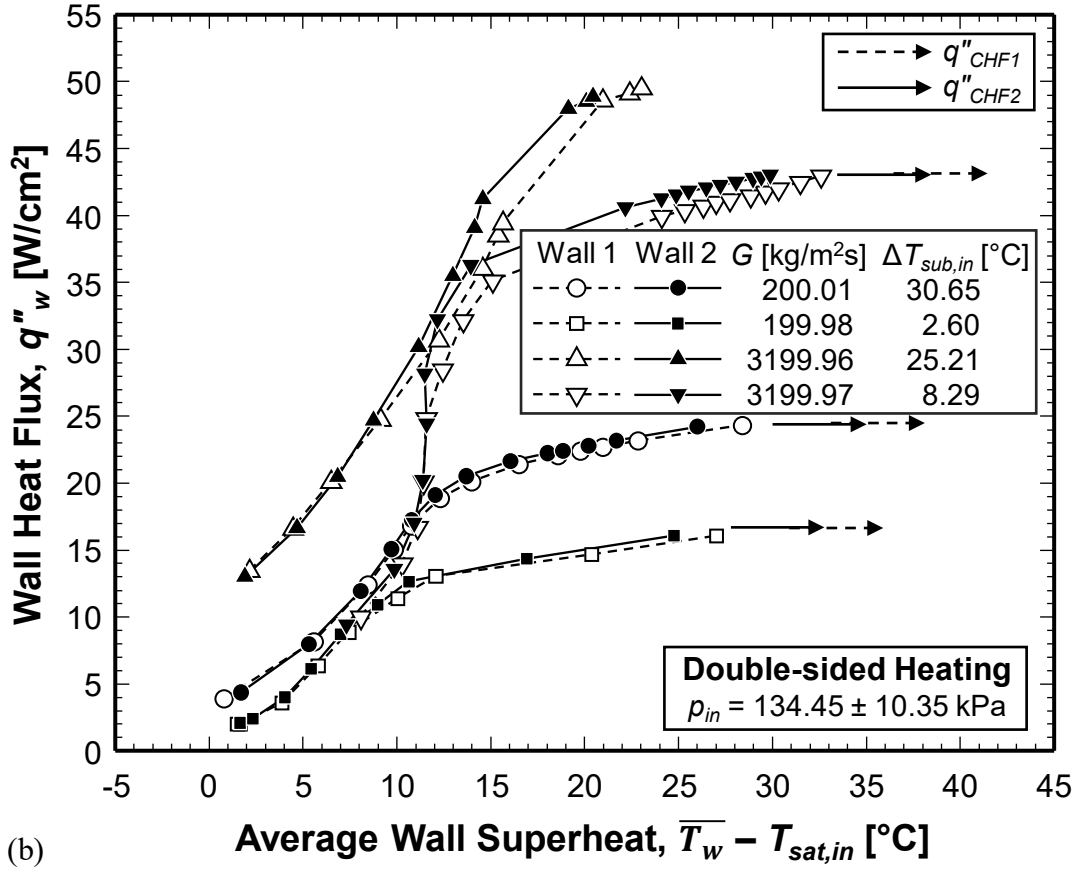

(b)

Fig. 13 Boiling curves illustrating the effects of fluid inlet subcooling at mass velocity extremes of $G = 200$ and 3200 kg/m^{2}s for (a) single-sided and (b) double-sided heating configurations .

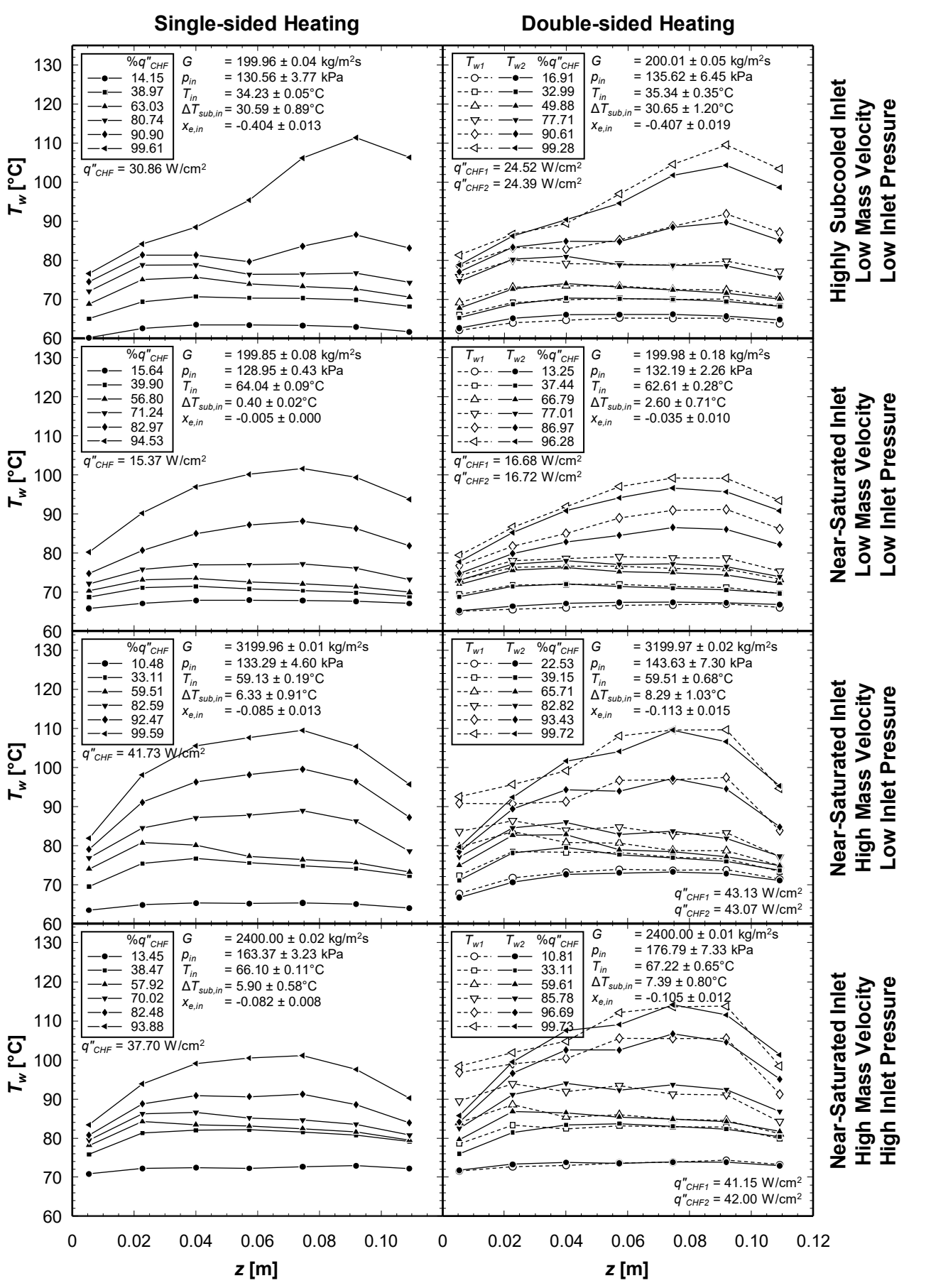

Fig. 14 Streamwise local wall temperature profiles for different heat fluxes with both single- and double-sided heating configurations at a variety of operating conditions.

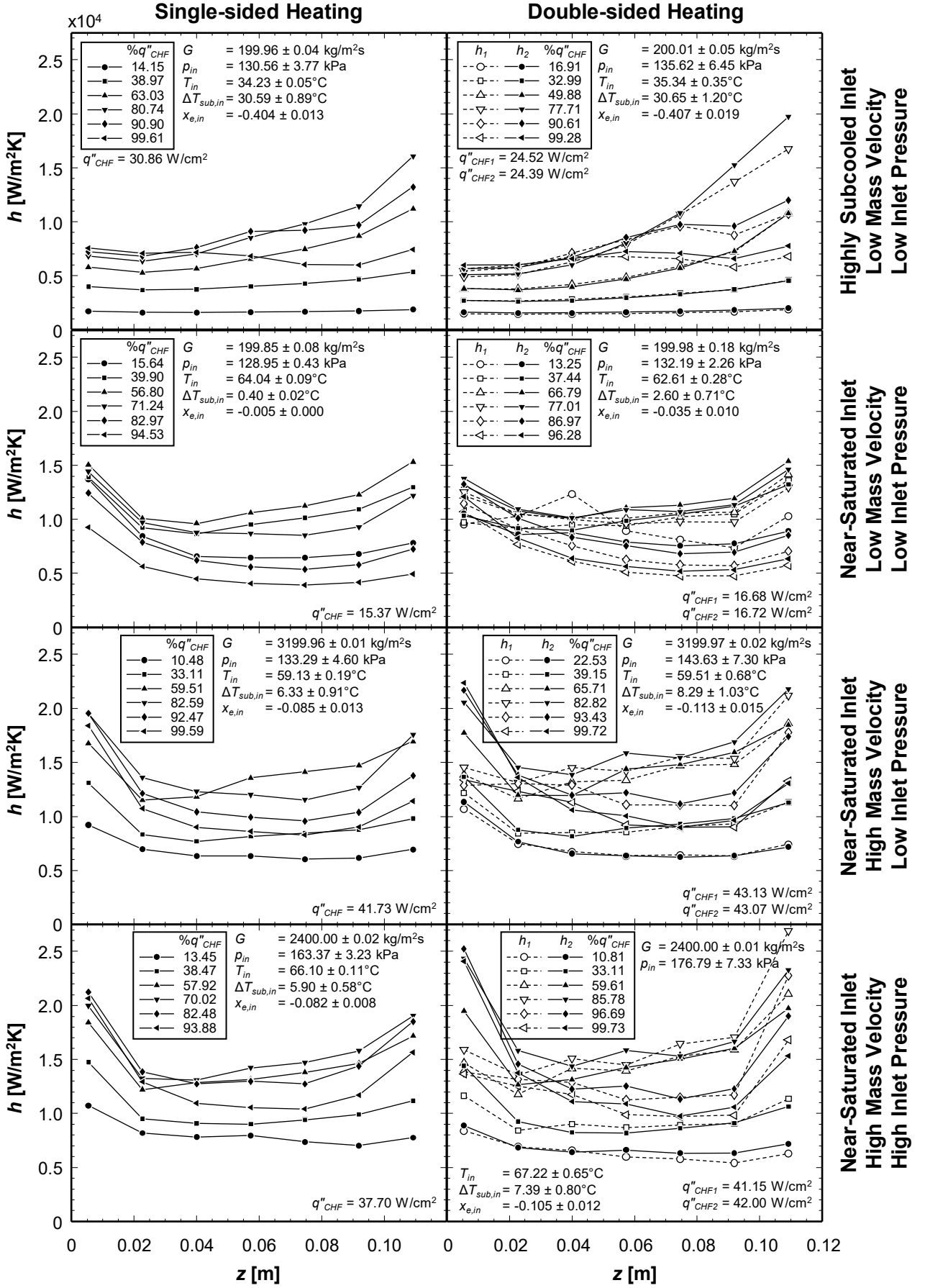

Fig. 15 Streamwise local heat transfer coefficient profiles for different heat fluxes with both single- and double-sided heating configurations at a variety of operating conditions.

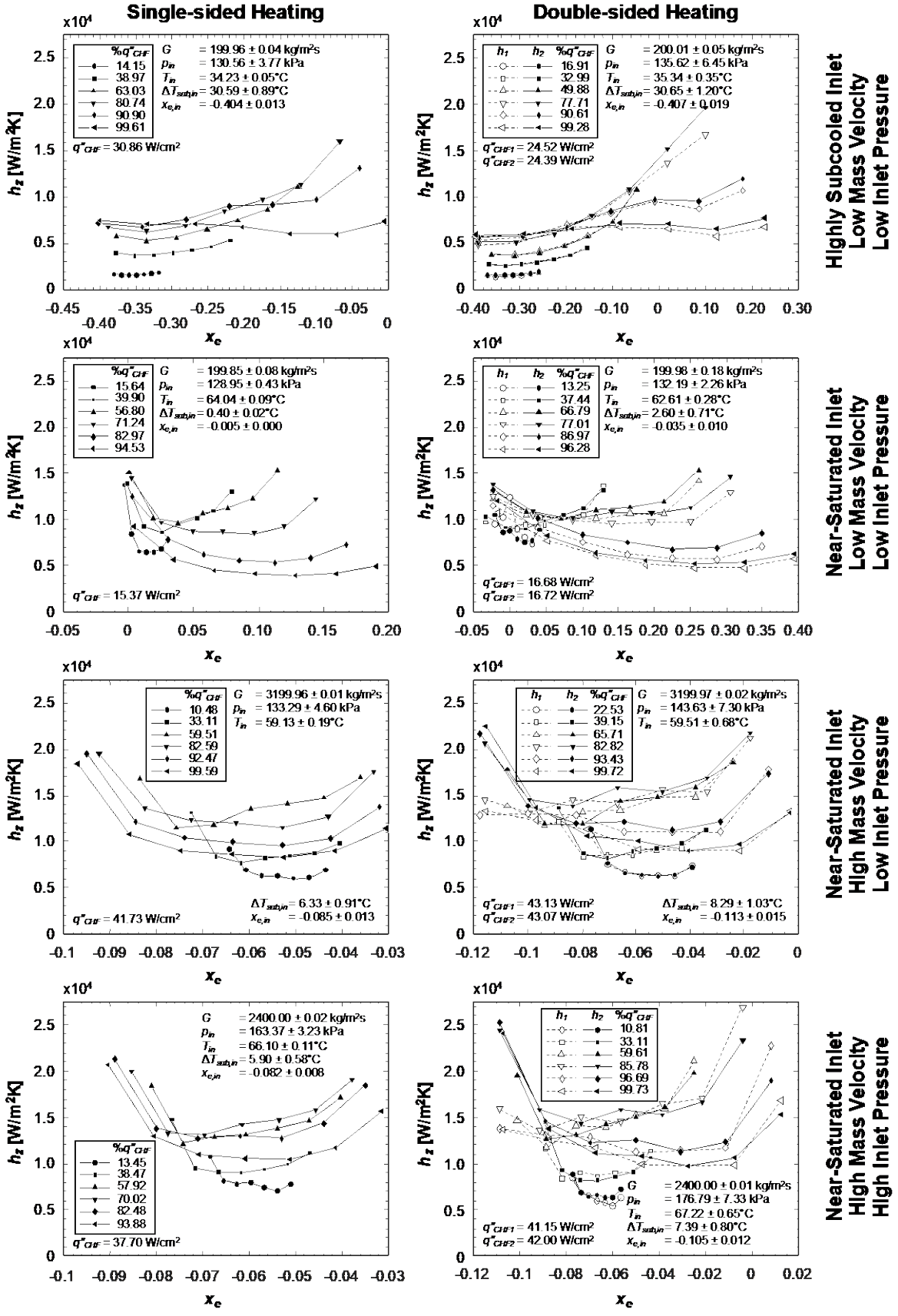

Fig. 16 Variations of local heat transfer coefficient with local thermodynamic equilibrium quality for different heat fluxes with both single- and double-sided heating configurations at a variety of operating conditions.

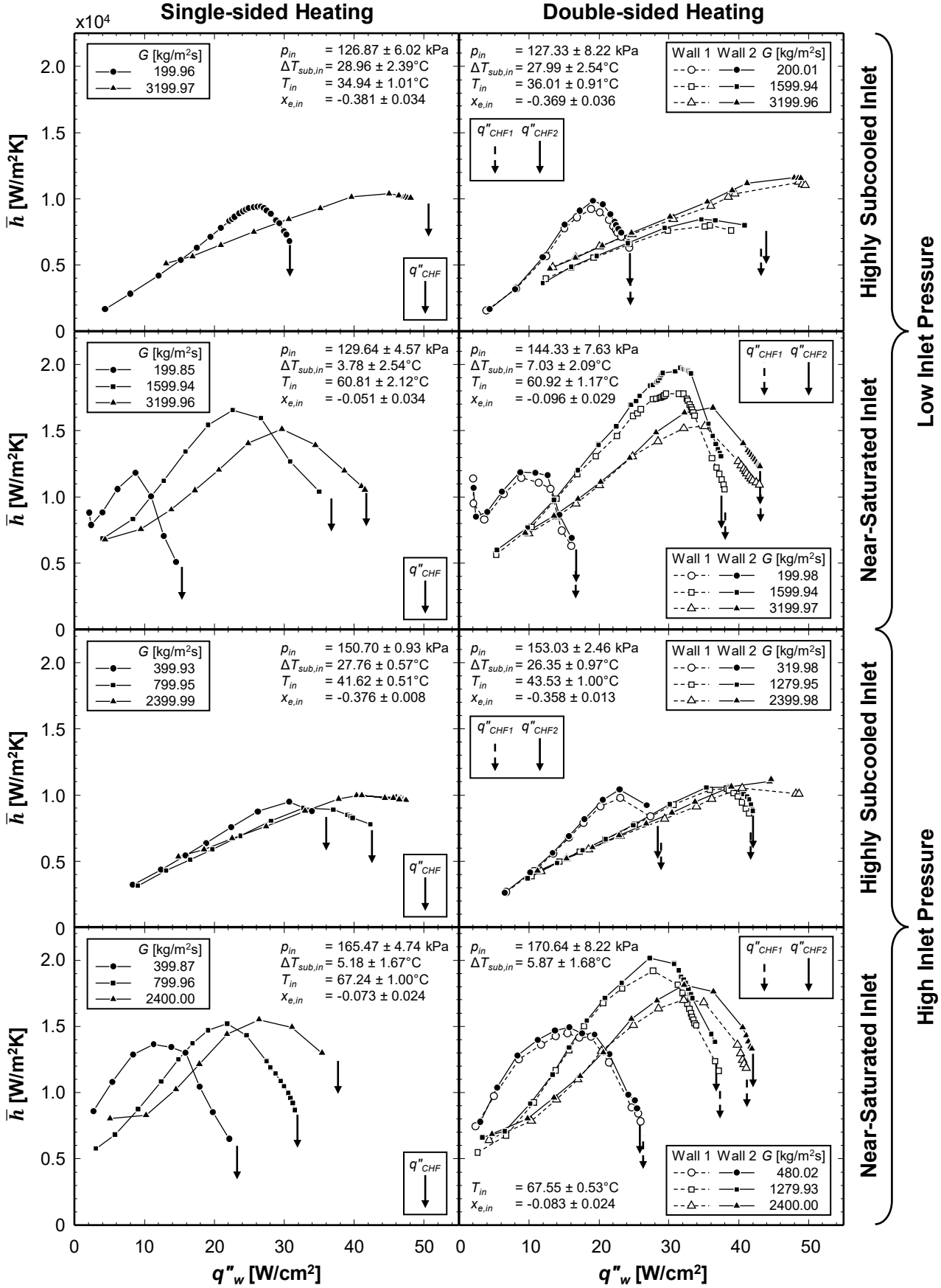

Fig. 17 Average heat transfer coefficient variations with wall heat flux for both single- and double-sided heating configurations at four different inlet conditions (two inlet subcoolings × two inlet pressures).